# Identifying a New Pathway for Nitrogen Reduction Reaction on Fe-doped $MoS_2$ by the Co-adsorption of Hydrogen and $N_2$

**Akash Jain,**[1] **Maya Bar Sadan**[2,3] **and Ashwin Ramasubramaniam**[4,*]

[1] Department of Chemical Engineering, University of Massachusetts, Amherst, MA 01003, U.S.A.

[2] Department of Chemistry Ben-Gurion University of the Negev, Beer-Sheva 8410501, Israel

[3] Ilse Katz Institute for Nanoscale Science and Technology, Ben-Gurion University of the Negev, Beer-Sheva 8410501, Israel

[4] Department of Mechanical and Industrial Engineering, University of Massachusetts, Amherst, MA 01003, U.S.A.

## ABSTRACT

The electrochemical nitrogen reduction reaction (NRR) is a promising alternative to the Haber-Bosch process with the potential for producing ammonia ($NH_3$) at ambient temperatures and pressures. Molybdenum disulfide ($MoS_2$), a layered transition-metal dichalcogenide, has attracted interest as an NRR electrocatalyst, but it possesses only a limited number of NRR-active sites and, furthermore, displays poor NRR selectivity due to the more favorable thermodynamics of the competing hydrogen evolution reaction (HER). To overcome these two challenges, we dope monolayer (ML) $MoS_2$ with iron (Fe) and employ density functional theory (DFT) calculations to investigate the nature of NRR-active defects and alternative reaction mechanisms. We show that Fe-doping can modify the structure of edges of $MoS_2$ MLs and assist in the formation of sulfur vacancy defects, which, in some cases, can selectively bind $N_2$ over protons. In a departure from current approaches to modeling NRR, we carefully consider the role of co-adsorbed H atoms, both at and in the vicinity of adsorption sites, and show how these competing adsorbates can profoundly affect both the preferred NRR pathways and their energetics. Our DFT studies reveal that a single sulfur vacancy on Fe-doped sulfur edges (50% S-coverage) can selectively reduce $N_2$ to $NH_3$ via a hitherto unexplored H-mediated enzymatic NRR pathway at moderate cathodic limiting potentials of 0.42 V. Our proposed H-mediated enzymatic NRR pathway shows that co-adsorbed H atoms can assist indirectly in the reduction of $N_2$ prior to the eventual evolution of $H_{2(g)}$. Our results suggest that Fe-doping of $MoS_2$ MLs is a promising approach for producing catalytic edge sites that are both active and selective for NRR at moderate potentials.

**Keywords:** Molybdenum disulfide, transition-metal dichalcogenides, heterogeneous catalysis, nitrogen reduction reaction, density functional theory

**Corresponding Author**

* ashwin@engin.umass.edu

## 1. INTRODUCTION

Ammonia ($NH_3$) is an important raw material for the chemical industry and a promising carbon-free fuel for fuel cells. Currently, the Haber-Bosch process is the standard approach for producing $NH_3$ from $N_2$ and $H_2$ over iron or ruthenium-based catalysts.[1,2] However, the Haber-Bosch process is energy-intensive, requires very high temperature (400°C-500°C) and pressure (~60 bar), and also generates an enormous amount of $CO_2$ and other greenhouse gases.[3] This high energy footprint of the Haber-Bosch process has motivated interest in electrochemical approaches for nitrogen reduction that can produce $NH_3$ at ambient temperature and pressure from electricity generated by renewable sources of energy. However, the lack of suitable electrocatalysts for the electrochemical nitrogen reduction reaction (NRR) presents an impediment to the widespread adoption of this approach. There are two major challenges in the design of NRR electrocatalysts: firstly, the $N_2$ molecule is difficult to activate owing to the highly stable $N\equiv N$ triple bond and, secondly, the NRR overpotential is larger than the competing hydrogen evolution reaction (HER) overpotential, which results in low NRR selectivity, especially in aqueous electrolytes.[4–6]

In nature, atmospheric $N_2$ fixation happens under ambient conditions on the nitrogenase enzyme in cyanobacteria, where the iron-molybdenum cofactor (FeMoco) is the active site for $N_2$ reduction.[7,8] To replicate FeMoco-like active sites in heterogeneous catalysts, several studies have explored Fe and Mo based catalysts like $FeS_2$,[9–11] FeS,[12], and $MoS_2$.[12–16] In particular, $MoS_2$, a two-dimensional layered transition-metal dichalcogenide (TMD), has attracted much attention as a potential NRR catalyst. The availability of NRR active edge sites, large catalytic surface area, high thermodynamic stability, and conductive nature of edges makes $MoS_2$ a promising catalyst for NRR.[13,14]

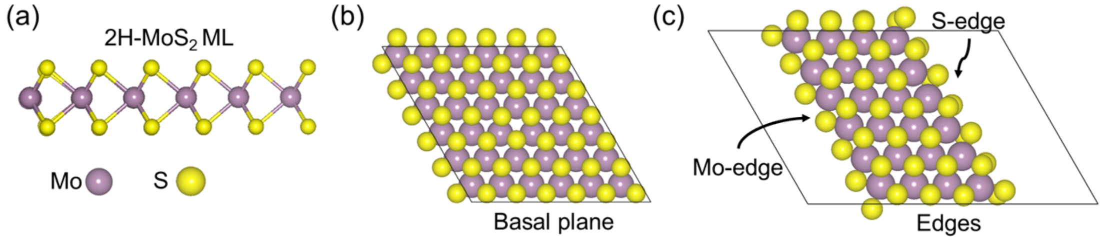

**Figure 1.** DFT models of (a) the $MoS_2$ ML, (b) defect-free $MoS_2$ ML basal plane, and (c) Mo-edge and S-edge of $MoS_2$ ML.

In the ground state, $MoS_2$ occurs in the semiconducting 2H phase. (Henceforth, we use $MoS_2$ generically to imply 2H-$MoS_2$.) Adsorption sites on $MoS_2$ monolayers (MLs) are available on the basal plane and edges (Figure 1). $MoS_2$ edges can be of two types—Mo-edges and S-edges—each with either partial or full sulfur coverage (edge termination). In ML $MoS_2$, the defect-rich basal plane and edges with low sulfur coverage typically expose under-coordinated Mo atoms that show excellent catalytic activity towards NRR.[13–15,17] Defect-free $MoS_2$ basal planes and edges with high sulfur coverage, on the other hand, are normally inert towards NRR because of the lack of exposed metal sites, leading to highly unfavorable adsorption thermodynamics of $N_2$ and other reaction intermediates.

In $MoS_2$ MLs, the basal planes, which constitute most of the exposed surface area, are inert and the active sites are limited to the edges. Introducing defects (like sulfur vacancies) or heteroatom dopants, and exposing more edges in the catalyst (e.g., through nano-structuring) can improve the activity of $MoS_2$ MLs. For example, density functional theory (DFT) studies have suggested anchoring single-atom catalysts and nanoclusters of transition-metal atoms, like Sc, Ti, Mo, Fe, Re, Zr, and Hf on defect-free and defect-rich $MoS_2$ ML to achieve better NRR selectivity and smaller NRR overpotential.[16,18–23] Zhang et al.[24] showed that substitutional doping with cobalt (Co) reduces the NRR overpotential and increases NRR selectivity of S-deficient $MoS_{2-x}$ nanoflowers. Zeng et al.[25,26] used Co and nitrogen (N) dopants to improve the NRR activity of $MoS_2$ nanoflowers. Despite this progress, the key issues of large NRR overpotential and low NRR selectivity for $MoS_2$ MLs remain open. To overcome these challenges, we need several under-coordinated metal-atom and S-vacancy sites on $MoS_2$ that can interact strongly with the inert $N_2$, so that electrochemical activation (or splitting) of the N≡N triple bond becomes more facile at low overpotentials.[13,15] However, these desirable active sites for NRR are also active for the competing HER at smaller overpotentials, which results in low NRR selectivity.[4,27,28] Therefore, for high NRR selectivity, we need to engineer active sites that either suppress HER or, minimally, allow for NRR at lower cathodic potentials than HER.

In this work, we employ DFT calculations to investigate comprehensively NRR on defect-rich iron (Fe) doped $MoS_2$ MLs. We chose Fe-doped $MoS_2$ because recent experiments reported significant improvement in HER and NRR catalytic activity of $MoS_2$ after Fe-doping, [22,29,30] although the mechanisms remain unclear. The remainder of this article is organized as follows. First, we characterize comprehensively the structure of Fe-doped $MoS_2$ ML edges based on thermodynamic considerations of edge formation energies. We calculate a phase diagram to determine the low-energy Fe-doped edge structures and show that Fe-doped edges of $MoS_2$ MLs are more stable than undoped $MoS_2$ edges. Thereafter, we study the energetics of introducing S-vacancy defects in these low-energy, Fe-doped edges, and identify defect sites that can selectively bind $N_2$ over protons to reduce $N_2$ to $NH_3$ at a low cathodic limiting potential. Finally, we study the reaction thermodynamics of NRR on selected Fe-doped edges and propose a new "H-mediated enzymatic pathway" in which co-adsorbed H atoms can participate in stabilizing NRR intermediates before eventually leaving the edge as $H_{2(g)}$. Overall, our work provides important insights into how and why Fe-doped $MoS_2$ displays higher NRR selectivity compared to undoped $MoS_2$, as reported in recent experiments,[22,29] and also underscores the importance of both cooperative and competing effects of protons in NRR.

## 2. COMPUTATIONAL METHODS

DFT calculations were performed using the Vienna Ab initio Simulation Package (VASP; version 5.4.1),[31,32] with spin-polarization to account for unpaired electrons of Fe dopant atoms. The projector-augmented wave (PAW) method was used to describe the core and valence electrons,[33,34] along with the Perdew-Burke-Ernzerhof (PBE) generalized gradient approximation (GGA) to describe electron exchange and correlation.[35] From convergence tests, the plane-wave cutoff energy was set to 400 eV and Gaussian smearing of 0.05 eV was chosen for integrations over the Brillouin zone. Structural optimization (atomic relaxation) was performed using the conjugate-gradient algorithm with a Hellman-Feynman force tolerance of 0.01 eV/Å. The $MoS_2$ ML basal plane (Figure 1(b)) was modeled using a 6 × 6 supercell with periodic boundary conditions (PBCs) applied within the plane of ML, and a vacuum region of 15 Å (chosen from convergence studies) was inserted normal to the plane to prevent interaction between the periodic images of the basal plane. The Brillouin zone was sampled using a 2 × 2 × 1 Γ-centered k-point mesh. Edge formation energies were calculated using triangular nanoflake models of $MoS_2$ MLs in which all three edges are identical, by construction (Figure S1).[39–41] Vacuum of 15 Å was inserted in all three Cartesian directions in these models; and a 1 × 1 × 1 Γ-point mesh was used. Similar to prior studies,[36–39] a nanoribbon model was used to study adsorption and reaction thermodynamics at edges of $MoS_2$ MLs (Figure 1(c)). The nanoribbon models were built using a 4 × 6 supercell of $MoS_2$ ML with PBCs applied along the longer in-plane direction (six unit cells); 15 Å of vacuum was inserted along the other in-plane direction (four unit cells), as well as in the direction normal to the basal plane, to minimize interactions between periodic images of the nanoribbon. A 1 × 2 × 1 Γ-centered k-point mesh was used to sample the Brillouin zones of the nanoribbons. It should be noted that the two parallel edges of the nanoribbon model represent two distinct $MoS_2$ edges—the Mo-edge and the S-edge. Thus, any edge formation energies calculated using a nanoribbon model will necessarily average over both dissimilar edges unlike the nanoflake model, which can be constructed to have only a single type of edge, allowing for unambiguous determination of the energy of that specific type of edge.[39] Dispersion interactions between atoms were modeled using the DFT-D3 method of Grimme *et al.*[42] The PBE (with DFT-D3) lattice parameter for an $MoS_2$ ML is 3.17 Å, which is close to the measured in-plane lattice parameter of bulk $MoS_2$ (3.16 Å [43]). The zero-point energy, defined as $E_{ZPE} = \sum_i \hbar\omega_i/2$ (where $\hbar$ is the reduced Planck's constant and $\omega_i$ is the atomic vibrational frequency), was calculated by displacing each atom from the equilibrium position by $\pm 0.015$ Å in all three Cartesian directions and diagonalizing the mass-weighted Hessian matrix to determine the vibrational frequencies $\omega_i$. From $\omega_i$, the vibrational entropy, *S_vib,* was estimated as,[44]

$$S_{vib} = k_B \sum_{i=1}^{N} \left[ -\ln\left(1 - e^{-\frac{\hbar\omega_i}{k_B T}}\right) + \frac{\hbar\omega_i/k_B T}{e^{\frac{\hbar\omega_i}{k_B T}} - 1} \right] \quad (1)$$

where $k_B$ is the Boltzmann constant, $T$ is the temperature (here, T=300 K), and $N$ is the total number of vibrational modes. The standard entropy of gas-phase $N_2$, $NH_3$, $H_2$, and $H_2S$ molecules were obtained from the NIST database.[45]

## 3. RESULTS AND DISCUSSION

### 3.1 Structure of Fe-doped Edges in $MoS_2$ MLs

First, we analyze $MoS_2$ edges, which usually display active sites for electrochemical reactions. To determine thermodynamically-favored edges of Fe-doped $MoS_2$ ML, we calculated the edge formation energy ($\gamma$), as a function of change in the chemical potential of sulfur relative to its bulk phase ($\Delta\mu_S = \mu_S - \mu_{S,bulk}$), using a triangular flake model of $MoS_2$ ML with three identical sides (or edges) of length $l$ (Figure 2(a)).[40,41] Details of the edge formation energy calculations are described in the SI.

For the undoped $MoS_2$ ML, previous studies have typically used Mo-edges with 100% (Mo100) and 50% (Mo50) sulfur coverage, and S-edges with 100% (S100) sulfur coverage.[41,46,47] Besides these edges, for the Fe-doped $MoS_2$ ML, we also studied the Mo-edge with 0% sulfur coverage (Mo0) and S-edges with 75% (S75) and 50% (S50) sulfur coverage (Figure S2). To understand better the effect of Fe-doping and dopant clustering on the structure and thermodynamic stability of these edges, we considered the

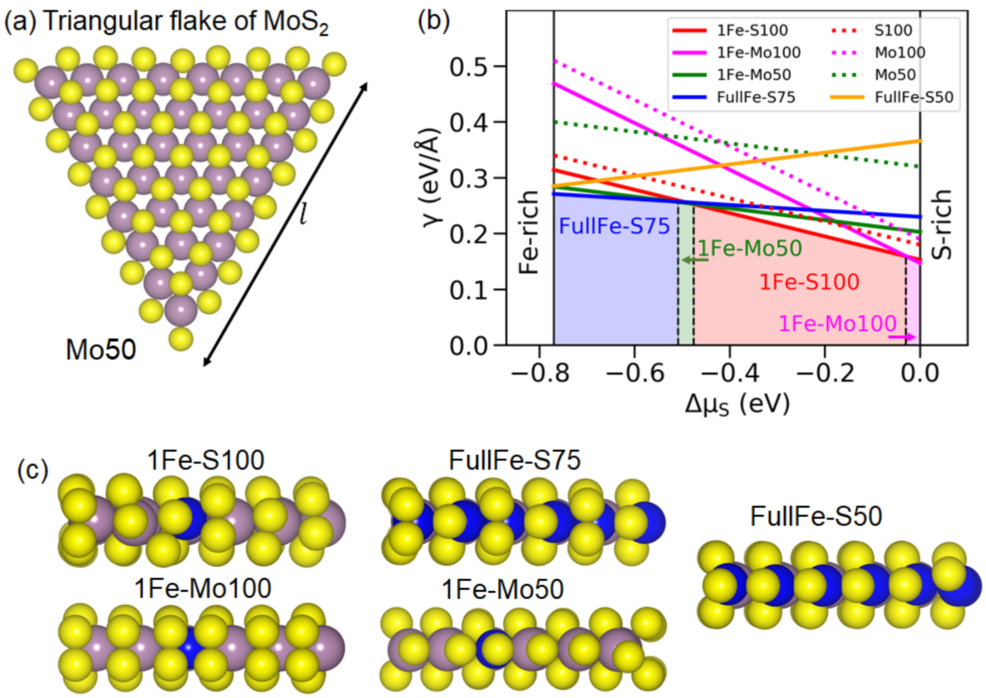

**Figure 2.** (a) Schematic of a triangular flake model of $MoS_2$ ML with side length $l$; the edges displayed are undoped Mo-edges with 50% S-coverage (Mo50). (b) Edge formation energy of select edges of undoped and Fe-doped $MoS_2$ as a function of change in chemical potential of sulfur. (c) Optimized structures of thermodynamically favored S-edges and Mo-edges of Fe-doped $MoS_2$ ML. Blue, yellow, and violet-gray spheres indicate Fe, S, and Mo atoms, respectively.

substitution of one, two, and all Mo atoms at the edge termination with Fe dopants.[21] In Figure 2(b), we display the edge formation energies of the aforementioned edges in undoped and Fe-doped $MoS_2$ ML as a function of $\Delta\mu_S$; Figure 2(c) displays the DFT-optimized structures of the four lowest-energy edges along with one additional edge (FullFe-S50) that is slightly higher in energy but important for the discussion that follows later in this article. As seen from Figure 2(b), by decreasing $\Delta\mu_S$, we move from the S-rich region to the Fe-rich region and alter the thermodynamic preference of the edge terminations. Close to the S-rich region ($-0.03 \text{ eV} < \Delta\mu_S < 0 \text{ eV}$), the Mo100 edge with one Fe dopant (1Fe-Mo100) is the thermodynamically preferred edge. Thereafter, within a large window ($-0.48\ \mathrm{eV} < \Delta\mu_S < -0.03\ \mathrm{eV}$), the S100 edge with one Fe-dopant (1Fe-S100) is favored. The Mo50 edge with 1Fe dopant (1Fe-Mo50) is energetically preferred within a small window of $-0.51\ \mathrm{eV} < \Delta\mu_S < -0.48\ \mathrm{eV}$, after which the fully doped S75 edge (FullFe-S75) becomes the most dominant edge within a broad window of $-0.77\ \mathrm{eV} < \Delta\mu_S < -0.51\ \mathrm{eV}$. It is noteworthy that all low-energy edges are seen to be Fe-doped, with pristine $MoS_2$ edges being much higher in energy. Given that it is desirable to stabilize edges with low sulfur coverage (below 50%) so that metal atoms at the edges become available for $N_2$ adsorption, we conclude that the sulfur chemical potential should be maintained at a low value ( $\Delta\mu_S < -0.5\ \mathrm{eV}$) to promote the formation of FullFe-S75 and 1Fe-Mo50 edges. It is also worth noting that the FullFe-S50 edge, which has even lower sulfur coverage, is very close in energy to the FullFe-S75 edge towards the Fe-rich regime (Figure 2(b)) and it may be possible to stabilize this edge during growth or produce this structure post-growth (e.g., by electrochemical etching). This reasoning is consistent with the results of Hong *et al.* [48] who studied full Fe-doped S-edges with 75% (FullFe-S75) and 50% (FullFe-S50) sulfur coverage for $CO_2$ reduction because of their similar thermodynamic stability.

### 3.2 $N_2$ and H Adsorption on Defect-Free Fe-doped $MoS_2$ ML Edges

Having ascertained the relevant low-energy edge terminations, we now examine the energetics of $N_2$ and H adsorption on all five selected Fe-doped $MoS_2$ ML edges. On defect-free edges, only sulfur sites are available for $N_2$ and H adsorption at the edges

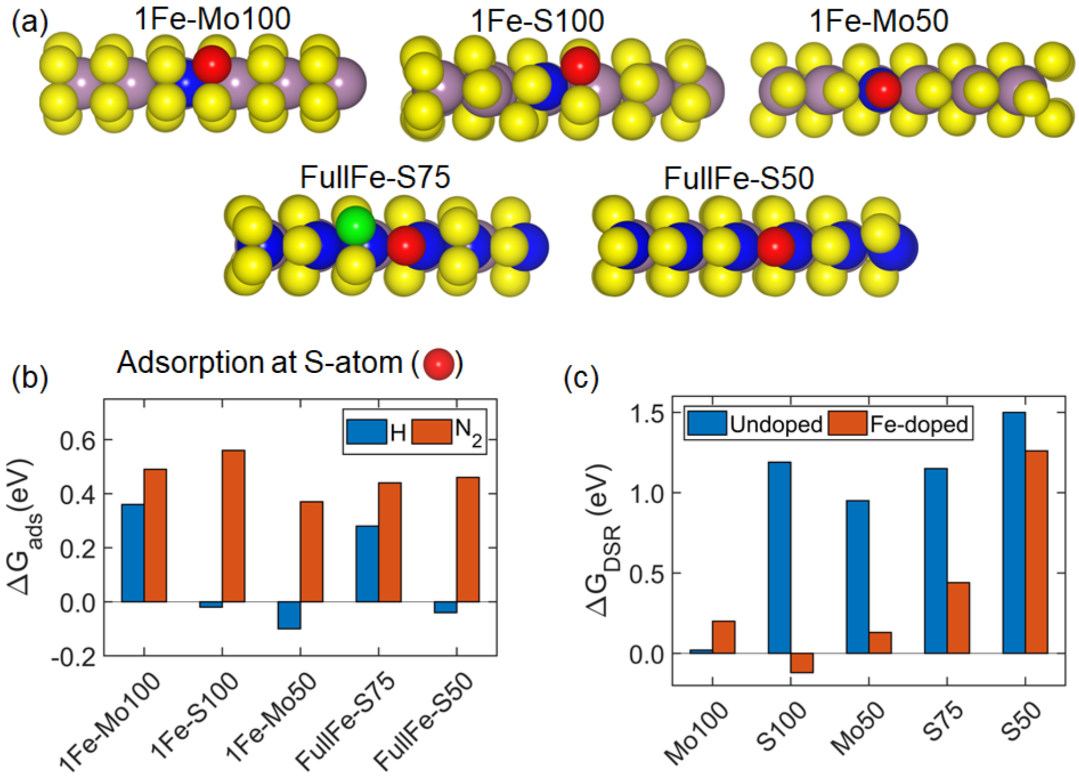

**Figure 3.** (a) Structures of Fe-doped $MoS_2$ ML edges: red spheres show the most favorable site (S atom) for H adsorption, and $N_2$ adsorption on Fe-doped $MoS_2$ ML edges; the green sphere on FullFe-S75 shows the most favorable site (S atom) for DSR; DSR on 1Fe-Mo100, 1Fe-S100, 1Fe-Mo50 and FullFe-S50 is most favorable at the H adsorption sites (red spheres). Gold, violet-grey, and yellow/red/green spheres represent the Fe, Mo, and S atoms, respectively. b) Free energy of H adsorption and $N_2$ adsorption at S atom sites on Fe-doped $MoS_2$ ML edges. (c) Free energy of DSR on all five selected Fe-doped $MoS_2$ ML edges and their respective undoped counterparts.

(Figure 3(a)). We define the free energy of $N_2$ ($\Delta G_{N_2}$) and H adsorption ($\Delta G_H$) on these sulfur edge sites as follows,

$$\Delta G_{N_2} = (E_{ML+N_2} - E_{N_2} - E_{ML}) + \Delta E_{ZPE} - T\Delta S, \quad (2)$$

$$\Delta G_H = (E_{ML+H} - 0.5 \times E_{H_2} - E_{ML}) + \Delta E_{ZPE} - T\Delta S, \quad (3)$$

where, $E_{ML}$, $E_{ML+N_2}$, $E_{ML+H}$, $E_{N_2}$, and $E_{H_2}$ are the 0K DFT energies of a clean ML, an ML with an adsorbed $N_2$ molecule, an ML with an adsorbed H atom, the isolated $N_2$ gas molecule, and the isolated $H_2$ gas molecule, respectively. $\Delta E_{ZPE}$ is the difference in zero-point energies of an ML with an adsorbed $N_2$ molecule/H atom and the reactants (clean ML and $N_{2\,(g)}$ or $1/2H_{2\,(g)}$) while $\Delta S$ is the corresponding difference in vibrational entropies. The temperature, T, is taken to be 300 K.

It is important to note that $N_2$ adsorption on the catalyst surface is a non-faradaic step, while H adsorption is a faradaic step. Hence, it is not possible to control $N_2$ adsorption thermodynamics during NRR with the applied cathodic potential.[49] Therefore, for efficient NRR and N≡N triple bond activation, the first step of $N_2$ adsorption should be thermodynamically favorable ($\Delta G_{N_2} \leq 0$) and preferred over H adsorption ($\Delta G_{N_2} < \Delta G_H$) to achieve NRR selectivity. However, from Figure 3(b), we find that $N_2$ adsorption at S atoms is consistently, and unsurprisingly, thermodynamically unfavorable with $\Delta G_{N_2} \sim 0.3 - 0.6$ eV, while the competing H adsorption (or HER) is consistently lower in energy and even exergonic in a few cases. Hence, we conclude that defect-free Fe-doped $MoS_2$ ML edges are not suited for NRR and only HER might occur in some instances.

### 3.3 Activation of Fe-doped $MoS_2$ ML Edges

Previous studies have shown that introducing defects in $MoS_2$ ML significantly improves the catalytic activity of $MoS_2$ ML for NRR.[13–15,17] Recently, Nørskov and coworkers[50] showed that active sulfur vacancies can be produced via the desulfurization reaction

(DSR) at large cathodic overpotentials. Specifically, DSR (Equation 4) proceeds in two steps (Equations 5 and 6):

$$^{*}S + 2(H^{+} + e^{-}) \rightarrow V_S + H_2S_{(g)} \tag{4}$$

$$^{*}S + (H^{+} + e^{-}) \rightarrow {}^{*}SH \tag{5}$$

$$^{*}SH + (H^{+} + e^{-}) \rightarrow V_S + H_2S_{(g)} \tag{6}$$

where $^{*}S$ represents the reacting S atom from $MoS_2$ and $V_S$ is the S vacancy site created after DSR. We note that Equation 5 is also the Volmer step of HER and so, DSR and HER are competing processes at the S atom site on $MoS_2$.[50] Once isolated sulfur vacancies or vacancy clusters are produced via DSR, the transition-metal atoms become accessible to reacting species and provide catalytic sites that are potentially more active and/or selective than pristine edges. Hence, for the activation of Fe-doped $MoS_2$ ML edges, it is necessary to understand the thermodynamics of DSR.

We investigated the thermodynamics of DSR to create a single $V_S$ site on Fe-doped $MoS_2$ ML edges and compared these results with the respective undoped edge case. Details of the free-energy calculations for DSR on $MoS_2$ edges, are described in the SI. We show the results of $\Delta G_{DSR}$ calculations of undoped and Fe-doped $MoS_2$ ML edges in Figure 3(c). On all Fe-doped $MoS_2$ ML edges (except the 1Fe-Mo100 edge), $\Delta G_{DSR}$ is smaller than the respective undoped $MoS_2$ ML edges. Smaller values of $\Delta G_{DSR}$ suggest that DSR is thermodynamically more favorable on Fe-doped $MoS_2$ ML edges than on undoped $MoS_2$ ML edges. This finding is consistent with our previous studies of DSR on $MoSe_2$ (a layered TMD with $MoS_2$ like crystal structure), where we found that DSR is more facile on transition-metal doped $MoSe_2$ ML than on undoped $MoSe_2$ ML.[51,52] Negative $\Delta G_{DSR}$ for the 1Fe-S100 case indicates that the formation of the sulfur vacancy is spontaneous. On 1Fe-Mo100 and 1Fe-Mo50 edges, $\Delta G_{DSR}$ is +0.18 eV and +0.13 eV, respectively, which suggests that $V_S$ formation can be accomplished at low cathodic potentials. FullFe-S75 and FullFe-S50 edges, on the other hand, have larger $\Delta G_{DSR}$ of +0.44 eV and +1.26 eV, respectively, requiring larger cathodic potentials for electrochemical etching.

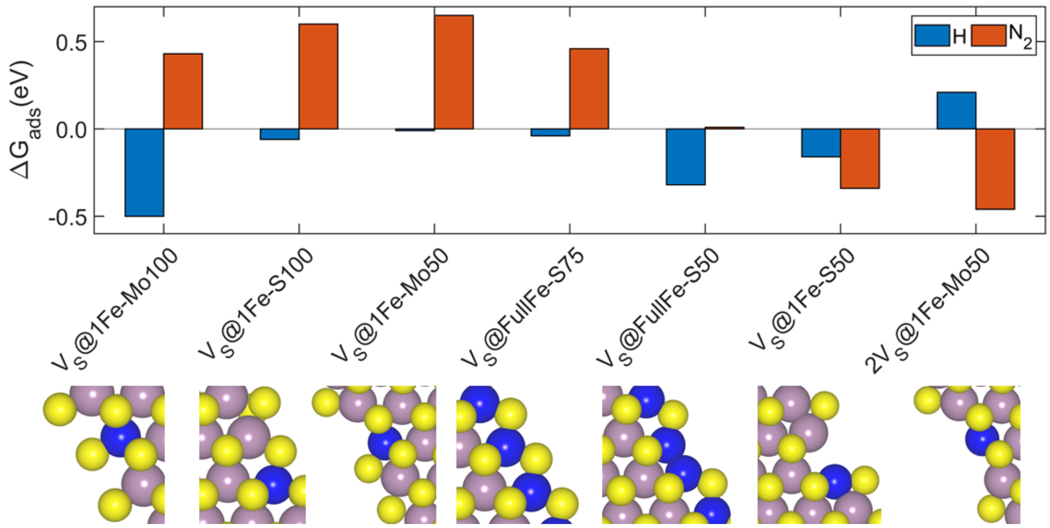

**Figure 4.** Free energies of H adsorption and $N_2$ adsorption on defect-rich Fe-doped $MoS_2$ ML edges. Structural models display the top view of the $V_S$@1Fe-Mo100, $V_S$@1Fe-S100, $V_S$@1Fe-Mo50, $V_S$@FullFe-S75, $V_S$@FullFe-S50, $V_S$@1Fe-S50 and $2V_S$@1Fe-Mo50 edges. Blue, violet-grey, and yellow spheres represent the Fe, Mo, and S atoms, respectively.

### 3.4 $N_2$ and H Adsorption on Defective Fe-doped $MoS_2$ ML Edges

A single $V_S$ site (on 1Fe-Mo100, 1Fe-S100, 1Fe-Mo50 or FullFe-S75), is less suitable for $N_2$ adsorption ($\Delta G_{N_2}$ > +0.45 eV), as seen in Figure 4, similarly to sulfur atoms on defect-free Fe-doped MoS2 ML edges. On the other hand, $V_S$ sites on the FullFe-S50 edge ($V_S$@FullFe-S50) with two exposed undercoordinated Fe-atoms show favorable thermodynamics for

$N_2$ adsorption with $\Delta G_{N_2} \approx 0$. However, undesirable H adsorption is still thermodynamically more favorable than $N_2$ adsorption ($\Delta G_H < \Delta G_{N_2}$) at all $V_S$ sites on these five selected Fe-doped edges. Thus, except for the $V_S$@FullFe-S50 case, we conclude that a single $V_s$ site is insufficient to activate Fe-doped edges, and $V_s$ clusters might be required to reduce the sulfur coverage below 50% and expose additional undercoordinated metal atoms. This could potentially be achieved by sustained electrochemical etching (multiple cycles of DSR) to introduce $V_s$ clusters along the Fe-doped edges. Specifically, on the two most dominant edges of Fe-doped $MoS_2$ ML—1Fe-S100 and FullFe-S75 (Figure 2(b))—one may envision reducing sulfur coverage, post-synthesis, by DSR to ≤50%, resulting in edges with exposed metal atoms ($V_S$@1Fe-S50 and $V_S$@FullFe-S50 in Figure 4). Also, removing two S atoms from 1Fe-Mo50 via multiple cycles of DSR will expose both Fe and Mo atoms and generate the $2V_S$@1Fe-Mo50 site (Figure 4). However, it should be noted that the formation of $V_S$ clusters on Fe-doped edges will require large cathodic potentials, because DSR thermodynamics ($\Delta G_{DSR} \geq 1$ eV) becomes less favorable on Fe-doped edges after the formation of the first single $V_S$ site (Figure S3). Large $\Delta G_{DSR}$ values also imply that under moderate cathodic potentials, DSR will not compete with HER and NRR at defect-rich Fe-doped $MoS_2$ edges. Hence, from this point forward we will only study HER and NRR on defect-rich Fe-doped $MoS_2$ edges.

From Figure 4, we note that $\Delta G_{N_2} < 0$ and $\Delta G_{N_2} < \Delta G_H$ at both $V_S$@1Fe-S50 and $2V_S$@1Fe-Mo50 sites and thus, these two sites will selectively adsorb $N_2$. For the $V_S$@FullFe-S50 edge, $N_2$ adsorption is nearly thermoneutral, although H adsorption is still preferred. In short, our calculations show that Fe-doped edges can indeed host defects or defect clusters that preferentially adsorb $N_2$ and this might explain the increased NRR selectivity of Fe-doped $MoS_2$ ML observed in recent experiments.[22,29] Going forward, for further investigation of NRR on Fe-doped $MoS_2$ ML edges, we only consider $V_S$@1Fe-S50, $V_S$@FullFe-S50, and $2V_S$@1Fe-Mo50 sites because these three sites display exergonic (or nearly thermoneutral) $N_2$ adsorption among all adsorption sites on Fe-doped $MoS_2$ ML edges that we considered here.[49] Parenthetically, we also investigated the Fe-doped $MoS_2$ ML basal plane, for completeness, and found that $\Delta G_{N_2} > +0.75\ \mathrm{eV}$ and $\Delta G_{N_2} > \Delta G_H$ on all S atom and $V_S$ sites (Figure S4) which means that $N_2$ adsorption is not favorable and only HER will occur on the Fe-doped $MoS_2$ basal plane.

### 3.5 NRR Mechanisms on Fe-doped $MoS_2$ ML Edges

In the literature,[15,53,54] it is generally assumed that electrochemical NRR [$N_{2(g)} + 6(H^+ + e^-) \rightarrow 2NH_{3(g)}$] on the catalyst surface occurs through the associative mechanism via distal, alternating, or enzymatic pathway (Figure 5). However, as discussed above, at most adsorption sites on the Fe-doped $MoS_2$ ML, H adsorption is thermodynamically more favorable than $N_2$ adsorption. Also, previous studies report that the NRR overpotential is generally larger than the HER overpotential.[4,5] Thus, it is reasonable to expect that during NRR on Fe-doped $MoS_2$, H atoms are co-adsorbed both at and in the vicinity of the adsorption site. Hence, apart from studying the conventional distal, alternating, and enzymatic pathways for NRR, we also chose to explore these (and closely related) pathways in the presence of co-adsorbed H atoms.

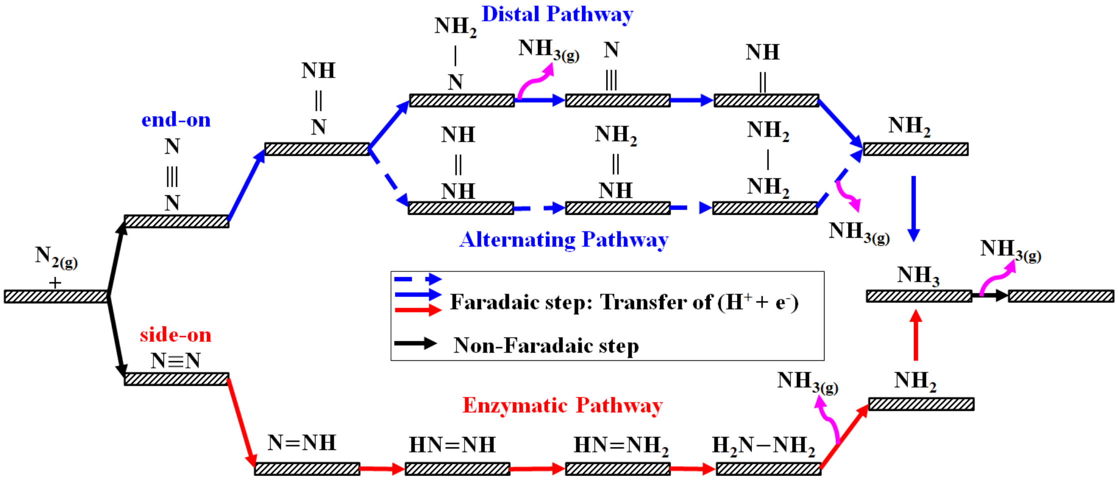

**Figure 5.** The associative distal, alternating, and enzymatic pathways of electrochemical NRR on a catalyst surface. Faradaic steps are connected by blue and red solid (or dashed) arrows, and non-faradic steps are connected by black solid arrows.

### 3.5.1 H-Mediated Enzymatic NRR Pathway on 1Fe-S50 Edge

We investigated NRR at the sulfur vacancy site on the 1Fe-S50 edge ($V_S$@1Fe-S50), which selectively binds $N_2$ ($\Delta G_{N_2} = -0.33$ eV; Figure 6). At the $V_S$@1Fe-S50 site, $N_2$ adsorption is side-on; therefore as per Figure 5, NRR is expected to proceed via the enzymatic pathway (Figure S7 and S8).[15,53,54] However, instead of subsequent direct protonation of the adsorbed $N_2$ molecule, we find that it is thermodynamically favorable to first co-adsorb three H atoms sequentially at neighboring Fe, S (adjacent to the Fe dopant), and Mo atoms to form $*N_2+*H$, $*N_2+2*H$, and $*N_2+3*H$ (Figure S7 and S8). The three initial H co-adsorption steps are still thermodynamically uphill (Figure 6). Thereafter, $*N_2$ (+3*H) is easily reduced to $*N_2H$ (+3*H) intermediate with ΔG = -0.02 eV. It should be noted that the alternative step, resulting in the formation of $*N_2+4*H$ with $\Delta G \approx 0$ (Figure S7 and S8) may be considered equally likely to within the accuracy of the calculation (~20 meV).

Nevertheless, starting from either $*N_2$+4*H or $*N_2H$+3*H, the subsequent protonation step results in the formation of the $*N_2H$+4*H with nearly similar reaction free energies (+0.22 eV and +0.24 eV), from which point on the reaction network remains the same. For the present discussion, we will assume that NRR proceeds via the $*N_2H$+3*H intermediate as $\Delta G < 0$.

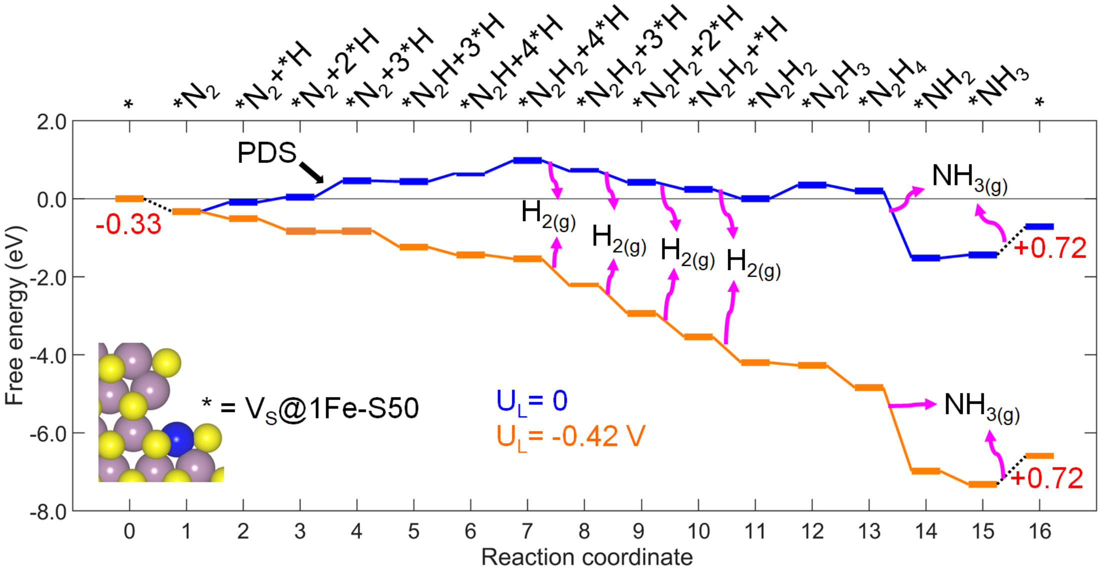

**Figure 6.** Free-energy diagram of the H-mediated enzymatic NRR pathway on $V_S$@1Fe-S50 at $U_L$=0 (blue) and $U_L$ = -0.42 V (orange), where $U_L$ is the applied (cathodic) limiting potential. Non-faradaic and faradaic reaction steps are connected by black (dashed) and blue/orange solid lines, respectively, and energies for the non-faradaic steps are indicated in the figure.

It is noteworthy that in the conventional enzymatic pathway the formation of the $*N_2H$ intermediate directly from $*N_2$ is substantially endergonic ($\Delta G$ = +0.55 eV; Figure S7(a)). Thus, a key difference between the conventional enzymatic pathway and the current one is revealed at the outset of the reduction process: firstly, none of the H co-adsorption steps are as endergonic as the direct protonation of $*N_2$ and, secondly, the eventual protonation of $*N_2$ (to form $*N_2H$+3*H) is slightly exergonic. In other words, H co-adsorption facilitates the reduction of $^*N_2$ to $^*N_2H$. We, therefore, refer to this pathway as the "H-mediated enzymatic pathway". After forming the $^*N_2H$ +3*H intermediate, the next protonation event occurs at the sulfur atom near the $V_S$@1Fe-S50 site to form $^*N_2H$+4*H ($\Delta G$ = +0.22 eV) followed by further protonation of the $^*N_2H$ intermediate to $^*N_2H_2$ ($\Delta G$ = +0.32 eV). At this point, the next four protonation steps result in HER and all four co-adsorbed H atoms desorb as $H_{2(g)}$ (exergonic) leaving behind only the $^*N_2H_2$ intermediate at the $V_S$@1Fe-S50 site. From this point on, the reaction follows the standard enzymatic pathway up to the formation of two ammonia molecules. Specifically, the liberation of the first ammonia molecule, leaving behind a $^*NH_2$ intermediate, is highly exergonic $\Delta G$ = -1.72 eV whereas the liberation of the second ammonia molecule requires +0.72 eV energy. It should be noted here that in actual experiments,[55–58] the likely outcome is the formation of a solvated $NH_4^+$ species, rather than the liberation of $NH_{3(g)}$, but this is not captured in the current DFT models and will be studied elsewhere.

In total, there are 16 reaction steps in the H-mediated enzymatic pathway proposed here, and the overall NRR reaction may be represented as $N_{2(g)} + 14(H^+ + e^-) \rightarrow 2NH_{3(g)} + 4H_{2(g)}$. Similar to the conventional enzymatic pathway, the first step ($N_2$ adsorption) and the last step ($NH_{3(g)}$ desorption) are non-faradaic steps while the remaining steps are faradaic. Compared to the standard enzymatic pathway ($N_{2(g)} + 6(H^+ + e^-) \rightarrow 2NH_{3(g)}$), the H-mediated enzymatic pathway consumes eight extra ($H^+$+$e^-$) pairs and generates four $H_{2(g)}$ molecules, which means that the maximum Faradaic Efficiency (FE) for $NH_3$ synthesis via the thermodynamically-favorable, H-mediated enzymatic pathway is ~43%. It is interesting to note that the H-mediated enzymatic NRR pathway resembles $N_2$ fixation by the iron-molybdenum cofactor in nitrogenase ($N_{2(g)} + 8(H^+ + e^-) \rightarrow 2NH_{3(g)} + H_{2(g)}$), wherein HER occurs in concert with NRR.[59]

In Figure 6, we display the free-energy diagram of NRR via the H-mediated enzymatic pathway at low cathodic overpotential ($U_L$ = 0). As seen from the reaction pathway, the formation of $*N_2$+3*H from $*N_2$+2*H (the fourth reaction step) is the most endergonic step (ΔG = +0.42 eV) among all faradaic steps and so we identify it as the potential determining step (PDS) of the reaction pathway. To assess the role of applied cathodic potentials on the reaction thermodynamics, we employed the computational hydrogen electrode (CHE) model[60] and estimated the cathodic limiting potential ($U_L$) relative to the reversible hydrogen electrode (RHE) required to make all faradaic steps of NRR exergonic ($\Delta G \leq 0$) on the $V_S$@1Fe-S50 site. In the CHE model, the reaction free energy change is given by $\Delta G = \Delta G^O - neU_L$, where $\Delta G^O$ is the standard free energy of a reaction step (at T=300 K), $n$ is the number of proton and electron pairs transferred during the reaction step, and $U_L$ is the applied cathodic limiting potential vs. RHE. Based on the calculated PDS, we require $U_L$ = -0.42 V to make all faradaic steps of the H-mediated enzymatic pathway exergonic. From Figure 6, we note that the thermodynamics of the first and sixteenth steps, which are non-faradaic, remain unaffected by the applied potential (within the assumptions of the CHE model). From Figure S7(b), we also note that for $U_L \leq$ -0.16 V, H adsorption (a faradaic step) becomes more favorable than $N_2$ adsorption at the $V_S$@1Fe-S50 site. Therefore, at larger cathodic potentials, the adsorbed H atom will block the $V_S$@1Fe-S50 site for $N_2$ adsorption and hinder NRR. The blocking of the $V_S$@1Fe-S50 site by H might play a role in the low NRR selectively of Fe-doped $MoS_2$ catalysts at large cathodic potentials reported in recent experiments.[22,29,30] Based on our results, it seems possible that NRR, using Fe-doped $MoS_2$ catalysts, may benefit from potential cycling approaches,[61,62] to selectively favor $N_2$ adsorption at low potentials and, thereafter, drive the reduction of $*N_2$ at higher potentials.

### *Role of Co-adsorbed H Atoms in $N_2$ Reduction*

**Table 1.** $*N_2$ bond length and charge gained by $*N_2$ adsorbed at the $V_S$@1Fe-S50 site with and without co-adsorbed H atoms

| **Adsorbed species** | **$*N_2$ bond length (Å)** | **Charge gained by $*N_2$ ($e^-$)** |
|---|---|---|
| Isolated $N_2$ | 1.11 | - |
| $*N_2$ | 1.16 | +0.50 |
| $*N_2 + *H$ | 1.16 | +0.50 |
| $*N_2 + 2\ *H$ | 1.16 | +0.50 |
| $*N_2 + 3\ *H$ | 1.17 | +0.54 |
| $*N_2 + 4\ *H$ | 1.18 | +0.63 |

To understand why the thermodynamics of the $*N_2$ to $*N_2H$ reduction step becomes more facile after the formation of $*N_2$+3*H and $*N_2$+4*H formation (Figure S7(a)) we examined structural change in $*N_2$ in the presence of co-adsorbed H structural as well as changes in the electronic structure of the adsorbate binding site with co-adsorbed H. In Table 1, we compared the bond lengths of adsorbed $*N_2$ molecule at the $V_S$@1Fe-S50 site with and without co-adsorbed H atoms. With no co-adsorbed H atoms, the $*N_2$ bond length is calculated to be 1.16 Å, which is larger than that calculated for the isolated $N_2$ molecule (1.11 Å), indicative of a more reactive $*N_2$ species. After co-adsorption of the first and second H atoms near the $V_S$@1Fe-S50 site, the $*N_2$ bond length remains unchanged (to within the accuracy of the calculation). In contrast, after the co-adsorption of the third and fourth H atoms, the $^*N_2$ bond further increases to 1.17 Å and 1.18 Å, respectively, which indicates further activation of the $^*N_2$ species (weaker bonding between N atoms). Furthermore, from a Bader charge analysis [63–65] (Table 1), we see that the $^*N_2$ molecule gains more electrons from the catalyst surface after the co-adsorption of the third and fourth H atoms (0.54 $e^-$ and 0.63 $e^-$, respectively), and this accumulation of additional electrons on the $^*N_2$ molecule results in additional electrostatic repulsion between the two N atoms, as reflected in the increased bond lengths.

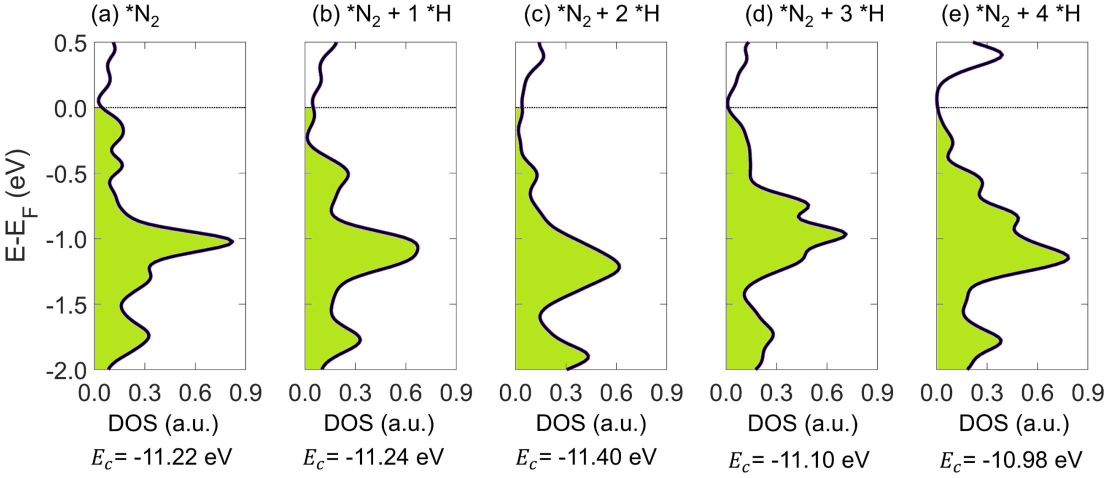

**Figure 7.** Calculated total density of states (DOS) of the adsorbed $N_2$ molecule around the Fermi level ($E_F$) at the $V_S$@1Fe-S50 site with (a) no, (b) one, (c) two (d) three and (e) four co-adsorbed H atoms. $E_C$ values below each panel indicate the average energy of the filled states of the adsorbed $N_2$ molecule relative to $E_F$. Green shaded regions show the filled states below $E_F$.

We also examined the evolution of the electronic density of states (DOS) of $^*N_2$ with the number of co-adsorbed H atoms (Figure 7). We estimated the average energy of the occupied electronic states ($E_C$) with respect to the Fermi Level ($E_F$) of the $^*N_2$ molecule as,

$$E_C = \frac{\int_{-\infty}^{E_F} E n_t(E) dE}{\int_{-\infty}^{E_F} n_t(E) dE} - E_F, \tag{7}$$

where $n_t(E)$ is the total DOS (sum of *s*- and *p*-projected states from both spin channels) of the $*N_2$ molecule at energy $E$. In the absence of co-adsorbed H, the average energy of the occupied states $*N_2$ is at $E_c$=-11.22 eV. Upon the co-adsorption of the first and second H atoms, we find that $E_C$ becomes more negative (i.e., shifts to lower energies values) and we also observe, qualitatively, a decrease in the DOS in the immediate vicinity of the Fermi level (Figure 7). Taken together, these two factors imply a less reactive $*N_2$ molecule. Thus, in the H-mediated enzymatic pathway, we observe no favorable changes in the thermodynamics of $N_2$ to $N_2H$ reduction steps after the co-adsorption of the first and second H atoms. In contrast, upon co-adsorption of the third and fourth H atoms, $E_C$ shifts up towards the Fermi level to higher energies values and we also observe an increase in the DOS near the Fermi level. Thus, the $*N_2$ species now becomes more reactive and this, in turn, is reflected in more favorable reaction thermodynamics for $*N_2$ protonation.

In short, we find that a combination of (interrelated) structural and electronic factors, arising from H co-adsorption, are responsible for activating the $*N_2$ species and making the H-mediated enzymatic pathway for NRR more favorable over the conventional enzymatic pathway.

### 3.5.2 Distal NRR pathway on FullFe-S50 Edge

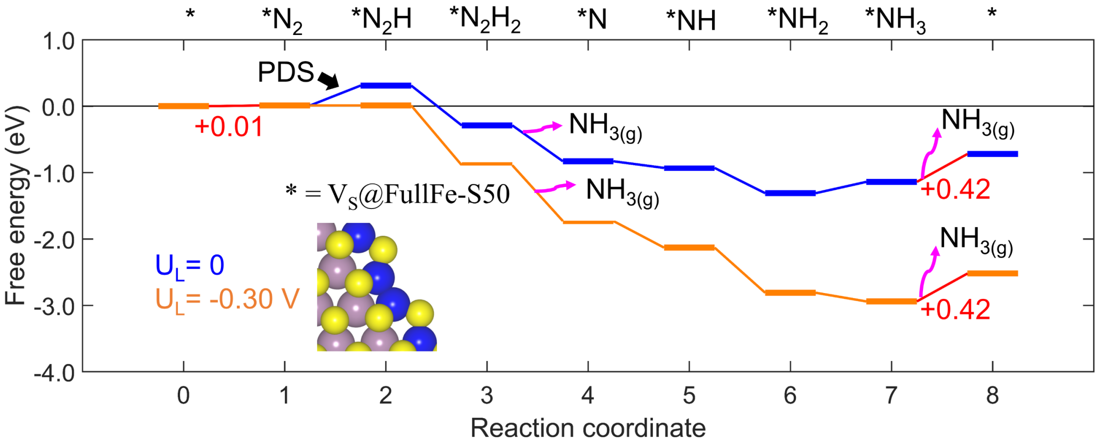

**Figure 8.** Free-energy diagram of the NRR on $V_S$@FullFe-S50 via the distal pathway at $U_L$=0 (blue) and $U_L$ = -0.30 V (orange), where $U_L$ is the applied (cathodic) limiting potential. Non-faradaic and faradaic reaction steps are connected by red and blue/orange solid lines, respectively, and energies for the non-faradaic steps are indicated in the figure.

As reported in Figure 4, $N_2$ adsorption at the $V_S$@FullFe-S50 site is nearly thermoneutral with $\Delta G_{N_2} = +0.01$ eV, and the $N_2$ molecule is adsorbed in a side-on configuration (Figures S9 and S10). While one may expect NRR to proceed via the enzymatic pathway, careful modeling reveals that $*N_2H$, $*N_2H_2$, and other reduced NRR intermediates turn out to be more stable in an end-on configuration (Figures S9 and S10), indicating that the side-on $*N_2$ species will switch to an end-on configuration upon protonation. Furthermore, we also investigated the NRR pathway with H atoms co-adsorbed near the $V_S$@FullFe-S50 site (Figures S9 and S10) but found that the H-mediated pathways are highly energetically unfavorable. Therefore, we only focus on the conventional distal pathway for NRR at the $V_S$@FullFe-S50 site.

In Figure 8, we display the free-energy diagram for NRR on the $V_S$@FullFe-S50 site at low overpotential ($U_L$=0). In the first step, $N_2$ adsorption (*$N_2$ formation) is nearly thermoneutral (ΔG = +0.01 eV). However, in the next step, the reduction of *$N_2$ to *$N_2H$ is uphill in energy (ΔG = +0.30 eV). After *$N_2H$ formation, the four subsequent steps leading to the formation of *$NH_2$ and $NH_{3(g)}$ are all downhill in energy. Further reduction of *$NH_2$ to *$NH_3$ and liberation of $NH_{3(g)}$ are uphill in energy with ΔG = +0.17 eV and ΔG = +0.42 eV, respectively. In this distal pathway, $N_2$ adsorption (the first step) and $NH_{3(g)}$ evolution (the last step) are non-faradaic steps, while all other steps are faradaic. Among the faradaic steps, the formation of *$N_2H$ from *$N_2$ (the second step) has the largest ΔG = +0.30 eV, which we identify as the PDS for this pathway. Thus, the $V_S$@FullFe-S50 site can, in principle, become NRR-active at moderately low $U_L$ of -0.30 V. However, from Figure 4, we also know that H adsorption is more favorable than $N_2$ adsorption on the $V_S$@FullFe-S50 site even at $U_L$=0 V ($\Delta G_H = -0.32$ eV and $\Delta G_{N_2} = +0.01\ \mathrm{eV}$. Furthermore, when $U_L$ = -0.30 V, the adsorption of a second H atom at the $V_S$@FullFe-S50 site also becomes more favorable than $N_2$ adsorption (Figure S9(b)). Thus, we expect that the $V_S$@FullFe-S50 is unlikely to be a good candidate for NRR.

### 3.5.3 Distal NRR pathway on 2$V_S$@1Fe-Mo50

The last site we consider is the 2$V_S$@lFe-Mo50 site, which selectively adsorbs $N_2$ at an exposed Fe-atom ($\Delta G_{N_2} = -0.46\ \mathrm{eV}$) in an end-on configuration (Figures S11 and S12). We find that NRR proceeds via the distal pathway on the 2$V_S$@lFe-Mo50 site (Figures S11 and S12). However, the reduction of adsorbed $N_2$ (*$N_2$) to *$N_2H$ intermediate is highly unfavorable and uphill in energy (ΔG = +1.14 eV). Further, the reduction of $*N_2H$ to $*N_2H_2$ is also uphill in energy (ΔG = +0.26 eV). Beyond this point (Figure 9), the process is thermodynamically downhill right until the final step of $NH_{3(g)}$, which is not spontaneous (ΔG = +0.46 eV). The PDS is thus determined by the reduction of $*N_2$ to $*N_2H$ and requires a rather large limiting potential, $U_L = -1.14$ V.

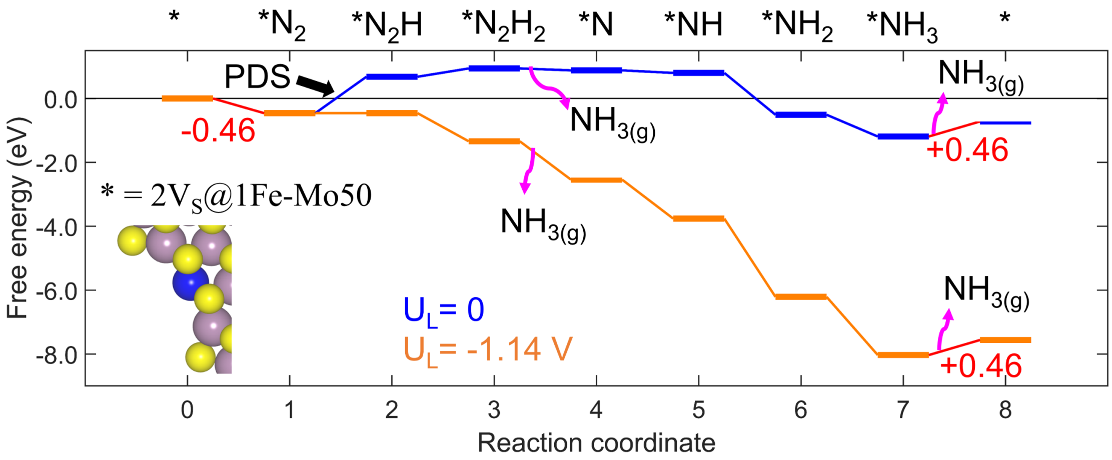

**Figure 9.** Free energy diagram of the NRR on $2V_S$@1Fe-Mo50 via the distal pathway, at $U_L$=0 (blue) and $U_L$ = -1.14 V (orange), where $U_L$ is applied limiting potential. Negative $U_L$ means the applied limiting potential is cathodic potential. Non-faradaic and faradaic reaction steps are connected by red and blue/orange solid lines, respectively, and energies for the non-faradaic steps are indicated in the figure.

For completeness, we also investigated NRR with co-adsorbed H atoms near the $2V_S$@lFe-Mo50 site (Figures S11(a) and S12) but the thermodynamics is still highly unfavorable due to the large energy input required for protonation of $*N_2$ to $*N_2H$. Additionally, from Figure S11(b), we also see that H adsorption is already more favorable than $N_2$ adsorption at $U_L \leq -0.67$ V, which is still insufficient to protonate $*N_2$. In short, the $2V_S$@lFe-Mo50 site is not particularly suited for NRR.

## 4. CONCLUSIONS

In conclusion, we employed DFT calculations to assess the potential of Fe-doped $MoS_2$ monolayers for electrochemical NRR. We found that placing Fe dopants at edges favors the formation of sulfur vacancies defects and, in the case of sulfur edges, their formation can even be spontaneous. Such vacancies or vacancy clusters can activate the Fe-doped $MoS_2$ ML for NRR by exposing metal atoms and facilitating $N_2$ adsorption. We studied the NRR mechanism and found that certain Fe-doped $MoS_2$ edge sites co-adsorb H and $N_2$, and that the vicinity of the two species offers a new reaction pathway, which we call "H-mediated enzymatic pathway", that resembles $N_2$ fixation by the iron-molybdenum cofactor in nitrogenase. In this new mechanism, the overall NRR reaction may be represented as $N_{2(g)} + 14(H^+ + e^-) \rightarrow 2NH_{3(g)} + 4H_{2(g)}$. Compared to the standard enzymatic pathway, $N_{2(g)} + 6(H^+ + e^-) \rightarrow 2NH_{3(g)}$, the H-mediated enzymatic pathway consumes eight extra $(H^+ + e^-)$ pairs and generates four $H_{2(g)}$ molecules. Hence, the H-mediated enzymatic pathway, while thermodynamically more favorable than the conventional enzymatic pathway, has a lower faradaic efficiency (~43%). In this H-mediated enzymatic pathway, H atoms that are co-adsorbed near the adsorption site assist in the activation of $*N_2$ and reduce the thermodynamic barrier for protonation of $*N_2$ to $*N_2H$, eventually leaving the edge as $H_{2(g)}$. While HER is likely to be favored at the larger potentials required to drive NRR, the fact that $N_2$ adsorption is preferred over H adsorption at low potentials suggests that it may be possible to dynamically modulate cathodic potential and drive selectivity towards NRR while reducing losses to the parasitic HER. Further, NRR selectivity of Fe-doped $MoS_2$ might improve by employing aprotic solvents to limit the availability of protons for parasitic HER and thereby increasing selectivity and faradaic efficiency for NRR.[4,5]

In summary, our results indicate that experimental observations[22,29] of higher NRR activity of Fe-doped $MoS_2$ based catalysts are likely to arise from sulfur vacancies associated with Fe dopants and that such defects associated with single Fe dopant atoms, rather than Fe dopant clusters, are more likely to be NRR active. Our studies also indicate that the role of co-adsorbed H atoms at and near these active sites, an aspect that is usually neglected in DFT models, ought to be considered more carefully and may even prove to be beneficial in assisting catalytic reactions. Besides H atoms, the role of the water molecules and adsorbed hydroxyl radicals should also be investigated as these species could compete for adsorption sites and block both HER and NRR. [66] Finally, we note that our present study is restricted to reaction thermodynamics, and it will be interesting to understand in the future how reaction kinetics (energy barriers) are affected by Fe-doping, by the presence of co-adsorbates, and by solvent effects.

## Supporting Information

Details of edge formation energy and electrochemical desulfurization reaction calculations for undoped and Fe-doped $MoS_2$ MLs; DSR, H and $N_2$ adsorption on the Fe-doped $MoS_2$ basal plane; Effect of Fe-doping on the electronic structure of $MoS_2$ edges; Reaction networks for various NRR pathways, with and without co-adsorbed H atoms, at various catalytic sites along with images of DFT-optimized structures; Free-energy diagrams of H and $N_2$ adsorption at selected applied cathodic potentials

## Acknowledgements

We gratefully acknowledge research support from the National Science Foundation (NSF-CBET-1803614) and the United States–Israel Binational Science Foundation (NSF-BSF CBET 2017642). This work used the Extreme Science and Engineering Discovery Environment (XSEDE), which is supported by National Science Foundation grant number ACI-1548562.

## REFERENCES

(1) Schlögl, R. Catalytic Synthesis of Ammonia—A “Never-Ending Story”? *Angew. Chemie Int. Ed.* **2003**, *42* (18), 2004–2008.

(2) Foster, S. L.; Bakovic, S. I. P.; Duda, R. D.; Maheshwari, S.; Milton, R. D.; Minteer, S. D.; Janik, M. J.; Renner, J. N.; Greenlee, L. F. Catalysts for Nitrogen Reduction to Ammonia. *Nat. Catal.* **2018**, *1* (7), 490–500.

(3) Bohnet, M. *Ullmann’s Encyclopedia of Industrial Chemistry*; Wiley-Vch, 2003.

(4) Singh, A. R.; Rohr, B. A.; Schwalbe, J. A.; Cargnello, M.; Chan, K.; Jaramillo, T. F.; Chorkendorff, I.; Nørskov, J. K. *Electrochemical Ammonia Synthesis—The Selectivity Challenge*. ACS Publications 2017.

(5) Singh, A. R.; Rohr, B. A.; Statt, M. J.; Schwalbe, J. A.; Cargnello, M.; Nørskov, J. K. Strategies toward Selective Electrochemical Ammonia Synthesis. *ACS Catal.* **2019**, *9* (9), 8316–8324.

(6) Légaré, M.-A.; Bélanger-Chabot, G.; Dewhurst, R. D.; Welz, E.; Krummenacher, I.;

Engels, B.; Braunschweig, H. Nitrogen Fixation and Reduction at Boron. *Science (80-. ).* **2018**, *359* (6378), 896–900.

(7) Burgess, B. K. The Iron-Molybdenum Cofactor of Nitrogenase. *Chem. Rev.* **1990**, *90* (8), 1377–1406.

(8) Shah, V. K.; Brill, W. J. Isolation of an Iron-Molybdenum Cofactor from Nitrogenase. *Proc. Natl. Acad. Sci.* **1977**, *74* (8), 3249–3253.

(9) Feng, D.; Zhang, X.; Sun, Y.; Ma, T. Surface-Defective $FeS_2$ for Electrochemical $NH_3$ Production under Ambient Conditions. *Nano Mater. Sci.* **2020**, *2* (2), 132–139.

(10) Lashgari, M.; Zeinalkhani, P. Ammonia Photosynthesis under Ambient Conditions Using an Efficient Nanostructured $FeS_2$/CNT Solar-Energy-Material with Water Feedstock and Nitrogen Gas. *Nano Energy* **2018**, *48*, 361–368.

(11) Wang, H.-B.; Wang, J.-Q.; Zhang, R.; Cheng, C.-Q.; Qiu, K.-W.; Yang, Y.; Mao, J.; Liu, H.; Du, M.; Dong, C.-K. Bionic Design of a Mo (IV)-Doped $FeS_2$ Catalyst for Electroreduction of Dinitrogen to Ammonia. *ACS Catal.* **2020**, *10* (9), 4914–4921.

(12) Guo, Y.; Yao, Z.; Timmer, B. J. J.; Sheng, X.; Fan, L.; Li, Y.; Zhang, F.; Sun, L. Boosting Nitrogen Reduction Reaction by Bio-Inspired FeMoS Containing Hybrid Electrocatalyst over a Wide pH Range. *Nano Energy* **2019**, *62*, 282–288.

(13) Matanovic, I.; Leung, K.; Percival, S. J.; Park, J. E.; Lu, P.; Atanassov, P.; Chou, S. S. Towards Defect Engineering in Hexagonal $MoS_2$ Nanosheets for Tuning Hydrogen Evolution and Nitrogen Reduction Reactions. *Appl. Mater. Today* **2020**, *21*, 100812.

(14) Zhang, L.; Ji, X.; Ren, X.; Ma, Y.; Shi, X.; Tian, Z.; Asiri, A. M.; Chen, L.; Tang, B.; Sun,

X. Electrochemical Ammonia Synthesis via Nitrogen Reduction Reaction on a $MoS_2$ Catalyst: Theoretical and Experimental Studies. *Adv. Mater.* **2018**, *30* (28), 1800191.

(15) Li, F.; Chen, L.; Liu, H.; Wang, D.; Shi, C.; Pan, H. Enhanced $N_2$-Fixation by Engineering the Edges of Two-Dimensional Transition-Metal Disulfides. *J. Phys. Chem. C* **2019**, *123* (36), 22221–22227.

(16) Azofra, L. M.; Sun, C.; Cavallo, L.; MacFarlane, D. R. Feasibility of $N_2$ Binding and Reduction to Ammonia on Fe-Deposited $MoS_2$ 2D Sheets: A DFT Study. *Chem. Eur. J.* **2017**, *23* (34), 8275–8279.

(17) Li, X.; Li, T.; Ma, Y.; Wei, Q.; Qiu, W.; Guo, H.; Shi, X.; Zhang, P.; Asiri, A. M.; Chen, L. Boosted Electrocatalytic $N_2$ Reduction to $NH_3$ by Defect-rich $MoS_2$ Nanoflower. *Adv. Energy Mater.* **2018**, *8* (30), 1801357.

(18) Zhai, X.; Li, L.; Liu, X.; Li, Y.; Yang, J.; Yang, D.; Zhang, J.; Yan, H.; Ge, G. A DFT Screening of Single Transition Atoms Supported on $MoS_2$ as Highly Efficient Electrocatalysts for the Nitrogen Reduction Reaction. *Nanoscale* **2020**, *12* (18), 10035–10043.

(19) Yang, T.; Song, T. T.; Zhou, J.; Wang, S.; Chi, D.; Shen, L.; Yang, M.; Feng, Y. P. High-Throughput Screening of Transition Metal Single Atom Catalysts Anchored on Molybdenum Disulfide for Nitrogen Fixation. *Nano Energy* **2020**, *68*, 104304.

(20) Zhao, J.; Zhao, J.; Cai, Q. Single Transition Metal Atom Embedded into a $MoS_2$ Nanosheet as a Promising Catalyst for Electrochemical Ammonia Synthesis. *Phys. Chem. Chem. Phys.* **2018**, *20* (14), 9248–9255.

(21) Guo, H.; Li, L.; Wang, X.; Yao, G.; Yu, H.; Tian, Z.; Li, B.; Chen, L. Theoretical Investigation on the Single Transition-Metal Atom-Decorated Defective $MoS_2$ for Electrocatalytic Ammonia Synthesis. *ACS Appl. Mater. Interfaces* **2019**, *11* (40), 36506–36514.

(22) Zhao, X.; Zhang, X.; Xue, Z.; Chen, W.; Zhou, Z.; Mu, T. Fe Nanodot-Decorated $MoS_2$ Nanosheets on Carbon Cloth: An Efficient and Flexible Electrode for Ambient Ammonia Synthesis. *J. Mater. Chem. A* **2019**, *7* (48), 27417–27422.

(23) Zhang, H.; Cui, C.; Luo, Z. $MoS_2$-Supported $Fe_2$ Clusters Catalyzing Nitrogen Reduction Reaction to Produce Ammonia. *J. Phys. Chem. C* **2020**, *124* (11), 6260–6266.

(24) Zhang, J.; Tian, X.; Liu, M.; Guo, H.; Zhou, J.; Fang, Q.; Liu, Z.; Wu, Q.; Lou, J. Cobalt-Modulated Molybdenum–Dinitrogen Interaction in $MoS_2$ for Catalyzing Ammonia Synthesis. *J. Am. Chem. Soc.* **2019**, *141* (49), 19269–19275.

(25) Zeng, L.; Chen, S.; van der Zalm, J.; Li, X.; Chen, A. Sulfur Vacancy-Rich N-Doped $MoS_2$ Nanoflowers for Highly Boosting Electrocatalytic $N_2$ Fixation to $NH_3$ under Ambient Conditions. *Chem. Commun.* **2019**, *55* (51), 7386–7389.

(26) Zeng, L.; Li, X.; Chen, S.; Wen, J.; Rahmati, F.; van der Zalm, J.; Chen, A. Highly Boosted Gas Diffusion for Enhanced Electrocatalytic Reduction of $N_2$ to $NH_3$ on 3D Hollow Co–$MoS_2$ Nanostructures. *Nanoscale* **2020**, *12* (10), 6029–6036.

(27) Hinnemann, B.; Moses, P. G.; Bonde, J.; Jørgensen, K. P.; Nielsen, J. H.; Horch, S.; Chorkendorff, I.; Nørskov, J. K. Biomimetic Hydrogen Evolution: $MoS_2$ Nanoparticles as Catalyst for Hydrogen Evolution. *J. Am. Chem. Soc.* **2005**, *127*

(15), 5308–5309.

(28) Tsai, C.; Abild-Pedersen, F.; Nørskov, J. K. Tuning the $MoS_2$ Edge-Site Activity for Hydrogen Evolution via Support Interactions. *Nano Lett.* **2014**, *14* (3), 1381–1387.

(29) Guo, J.; Tsega, T. T.; Islam, I. U.; Iqbal, A.; Zai, J.; Qian, X. Fe Doping Promoted Electrocatalytic $N_2$ Reduction Reaction of 2H $MoS_2$. *Chinese Chem. Lett.* **2020**, *31* (9), 2487–2490.

(30) Xue, J.-Y.; Li, F.-L.; Zhao, Z.-Y.; Li, C.; Ni, C.-Y.; Gu, H.-W.; Young, D. J.; Lang, J.-P. In Situ Generation of Bifunctional Fe-Doped $MoS_2$ Nanocanopies for Efficient Electrocatalytic Water Splitting. *Inorg. Chem.* **2019**, *58* (16), 11202–11209.

(31) Kresse, G.; Furthmüller, J. Efficient Iterative Schemes for Ab Initio Total-Energy Calculations Using a Plane-Wave Basis Set. *Phys. Rev. B* **1996**, *54* (16), 11169–11186.

(32) Kresse, G.; Furthmüller, J. Efficiency of Ab-Initio Total Energy Calculations for Metals and Semiconductors Using a Plane-Wave Basis Set. *Comput. Mater. Sci.* **1996**, *6* (1), 15–50.

(33) Blöchl, P. E. Projector Augmented-Wave Method. *Phys. Rev. B* **1994**, *50* (24), 17953–17979.

(34) Kresse, G.; Joubert, D. From Ultrasoft Pseudopotentials to the Projector Augmented-Wave Method. *Phys. Rev. B* **1999**, *59* (3), 1758–1775.

(35) Perdew, J. P.; Burke, K.; Ernzerhof, M. Generalized Gradient Approximation Made Simple. *Phys. Rev. Lett.* **1996**, *77* (18), 3865–3868.

(36) Bollinger, M. V; Jacobsen, K. W.; No, J. K.; Mos, E. Atomic and Electronic Structure

of $MoS_2$ Nanoparticles. **2003**, No. June 2002, 1–17.

(37) Byskov, L. S.; Nørskov, J. K.; Clausen, B. S.; Topsøe, H. DFT Calculations of Unpromoted and Promoted $MoS_2$-Based Hydrodesulfurization Catalysts. *J. Catal.* **1999**, *187* (1), 109–122.

(38) Bollinger, M. V; Lauritsen, J. V; Jacobsen, K. W.; Nørskov, J. K.; Helveg, S.; Besenbacher, F. One-Dimensional Metallic Edge States in $MoS_2$. *Phys. Rev. Lett.* **2001**, *87* (19), 196803.

(39) Deng, J.; Fampiou, I.; Liu, J. Z.; Ramasubramaniam, A.; Medhekar, N. V. Edge Stresses of Non-Stoichiometric Edges in Two-Dimensional Crystals. *Appl. Phys. Lett.* **2012**, *100* (25), 251906.

(40) Li, T.; Galli, G. Electronic Properties of $MoS_2$ Nanoparticles. *J. Phys. Chem. C* **2007**, *111* (44), 16192–16196.

(41) Cao, D.; Shen, T.; Liang, P.; Chen, X.; Shu, H. Role of Chemical Potential in Flake Shape and Edge Properties of Monolayer $MoS_2$. *J. Phys. Chem. C* **2015**, *119* (8), 4294–4301.

(42) Grimme, S.; Antony, J.; Ehrlich, S.; Krieg, H. A Consistent and Accurate Ab Initio Parametrization of Density Functional Dispersion Correction (DFT-D) for the 94 Elements H-Pu. *J. Chem. Phys.* **2010**, *132* (15), 154104.

(43) Young, P. A. Lattice Parameter Measurements on Molybdenum Disulphide. *J. Phys. D. Appl. Phys.* **1968**, *1* (7), 936.

(44) Brehm, G.; Reiher, M.; Schneider, S. Estimation of the Vibrational Contribution to the Entropy Change Associated with the Low-to High-Spin Transition in

$Fe(Phen)_2(NCS)_2$ Complexes: Results Obtained by IR and Raman Spectroscopy and DFT Calculations. *J. Phys. Chem. A* **2002**, *106* (50), 12024–12034.

(45) Johnson III, R. D. *NIST 101. Computational Chemistry Comparison and Benchmark Database*; 1999.

(46) Lauritsen, J. V; Bollinger, M. V; Lægsgaard, E.; Jacobsen, K. W.; Nørskov, J. K.; Clausen, B. S.; Topsøe, H.; Besenbacher, F. Atomic-Scale Insight into Structure and Morphology Changes of $MoS_2$ Nanoclusters in Hydrotreating Catalysts. *J. Catal.* **2004**, *221* (2), 510–522.

(47) Chan, K.; Tsai, C.; Hansen, H. A.; Nørskov, J. K. Molybdenum Sulfides and Selenides as Possible Electrocatalysts for $CO_2$ Reduction. *ChemCatChem* **2014**, *6* (7), 1899–1905.

(48) Hong, X.; Chan, K.; Tsai, C.; Nørskov, J. K. How Doped $MoS_2$ Breaks Transition-Metal Scaling Relations for $CO_2$ Electrochemical Reduction. *ACS Catal.* **2016**, *6* (7), 4428–4437.

(49) Choi, J.; Suryanto, B. H. R.; Wang, D.; Du, H.-L.; Hodgetts, R. Y.; Vallana, F. M. F.; MacFarlane, D. R.; Simonov, A. N. Identification and Elimination of False Positives in Electrochemical Nitrogen Reduction Studies. *Nat. Commun.* **2020**, *11* (1), 1–10.

(50) Tsai, C.; Li, H.; Park, S.; Park, J.; Han, H. S.; Nørskov, J. K.; Zheng, X.; Abild-Pedersen, F. Electrochemical Generation of Sulfur Vacancies in the Basal Plane of $MoS_2$ for Hydrogen Evolution. *Nat. Commun.* **2017**, *8*, 15113.

(51) Kuraganti, V.; Jain, A.; Bar-Ziv, R.; Ramasubramaniam, A.; Bar-Sadan, M. Manganese Doping of $MoSe_2$ Promotes Active Defect Sites for Hydrogen

Evolution. *ACS Appl. Mater. Interfaces 11* (28), 25155–25162.

(52) Jain, A.; Sadan, M. B.; Ramasubramaniam, A. Promoting Active Sites for Hydrogen Evolution in $MoSe_2$ via Transition-Metal Doping . *J. Phys. Chem. C* **2020**, *124* (23), 12324–12336.

(53) Anderson, J. S.; Cutsail III, G. E.; Rittle, J.; Connor, B. A.; Gunderson, W. A.; Zhang, L.; Hoffman, B. M.; Peters, J. C. Characterization of an $Fe\equiv N–NH_2$ Intermediate Relevant to Catalytic $N_2$ Reduction to NH3. *J. Am. Chem. Soc.* **2015**, *137* (24), 7803–7809.

(54) Li, X.-F.; Li, Q.-K.; Cheng, J.; Liu, L.; Yan, Q.; Wu, Y.; Zhang, X.-H.; Wang, Z.-Y.; Qiu, Q.; Luo, Y. Conversion of Dinitrogen to Ammonia by $FeN_3$-Embedded Graphene. *J. Am. Chem. Soc.* **2016**, *138* (28), 8706–8709.

(55) Hodgetts, R. Y.; Kiryutin, A. S.; Nichols, P.; Du, H.-L.; Bakker, J. M.; Macfarlane, D. R.; Simonov, A. N. Refining Universal Procedures for Ammonium Quantification via Rapid 1H NMR Analysis for Dinitrogen Reduction Studies. *ACS Energy Lett.* **2020**, *5* (3), 736–741.

(56) Bobroff, S.; Phillips, R. J.; Shekarriz, A. *Nuclear Magnetic Resonance Measurement of Ammonia Diffusion in Dense Solid-Liquid Slurries. Revision 1*; Pacific Northwest National Lab., 1998.

(57) Li, C.; Wang, T.; Zhao, Z.; Yang, W.; Li, J.; Li, A.; Yang, Z.; Ozin, G. A.; Gong, J. Promoted Fixation of Molecular Nitrogen with Surface Oxygen Vacancies on Plasmon-enhanced $TiO_2$ Photoelectrodes. *Angew. Chemie Int. Ed.* **2018**, *57* (19), 5278–5282.

(58) Chen, S.; Liu, D.; Peng, T. Fundamentals and Recent Progress of Photocatalytic Nitrogen-Fixation Reaction over Semiconductors. *Sol. Rrl* **2021**, *5* (2), 2000487.

(59) Hoffman, B. M.; Lukoyanov, D.; Yang, Z.-Y.; Dean, D. R.; Seefeldt, L. C. Mechanism of Nitrogen Fixation by Nitrogenase: The next Stage. *Chem. Rev.* **2014**, *114* (8), 4041–4062.

(60) Nørskov, J. K.; Rossmeisl, J.; Logadottir, A.; Lindqvist, L.; Kitchin, J. R.; Bligaard, T.; Jónsson, H. Origin of the Overpotential for Oxygen Reduction at a Fuel-Cell Cathode. *J. Phys. Chem. B* **2004**, *108* (46), 17886–17892.

(61) Shetty, M.; Walton, A.; Gathmann, S. R.; Ardagh, M. A.; Gopeesingh, J.; Resasco, J.; Birol, T.; Zhang, Q.; Tsapatsis, M.; Vlachos, D. G. The Catalytic Mechanics of Dynamic Surfaces: Stimulating Methods for Promoting Catalytic Resonance. *ACS Catal.* **2020**, *10* (21), 12666–12695.

(62) Gopeesingh, J.; Ardagh, M. A.; Shetty, M.; Burke, S. T.; Dauenhauer, P. J.; Abdelrahman, O. A. Resonance-Promoted Formic Acid Oxidation via Dynamic Electrocatalytic Modulation. *ACS Catal.* **2020**, *10* (17), 9932–9942.

(63) Tang, W.; Sanville, E.; Henkelman, G. A Grid-Based Bader Analysis Algorithm without Lattice Bias. *J. Phys. Condens. Matter* **2009**, *21* (8), 84204.

(64) Henkelman, G.; Arnaldsson, A.; Jónsson, H. A Fast and Robust Algorithm for Bader Decomposition of Charge Density. *Comput. Mater. Sci.* **2006**, *36* (3), 354–360.

(65) Sanville, E.; Kenny, S. D.; Smith, R.; Henkelman, G. Improved Grid-based Algorithm for Bader Charge Allocation. *J. Comput. Chem.* **2007**, *28* (5), 899–908.

(66) Abidi, N.; Bonduelle-Skrzypczak, A.; Steinmann, S. N. Revisiting the Active Sites at

the $MoS_2$/$H_2O$ Interface via Grand-Canonical DFT: The Role of Water Dissociation. *ACS Appl. Mater. Interfaces* **2020**, *12* (28), 31401–31410.

## Table of Contents Figure

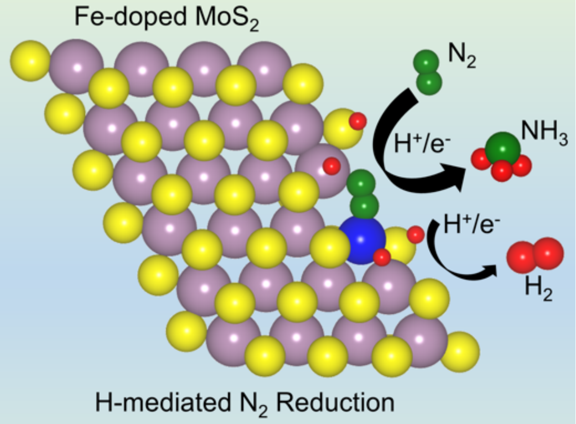

**SUPPLEMENTARY INFORMATION**

# Identifying a New Pathway for Nitrogen Reduction Reaction on Fe-doped $MoS_2$ by the Co-adsorption of Hydrogen and $N_2$

**Akash Jain,**[1] **Maya Bar Sadan**[2,3] **and Ashwin Ramasubramaniam**[4,*]

[1] Department of Chemical Engineering, University of Massachusetts, Amherst, MA 01003, U.S.A.

[2] Department of Chemistry Ben-Gurion University of the Negev, Beer-Sheva 8410501, Israel

[3] Ilse Katz Institute for Nanoscale Science and Technology, Ben-Gurion University of the Negev, Beer-Sheva 8410501, Israel

[4] Department of Mechanical and Industrial Engineering, University of Massachusetts, Amherst, MA 01003, U.S.A.

## Edge Formation Energy Calculation

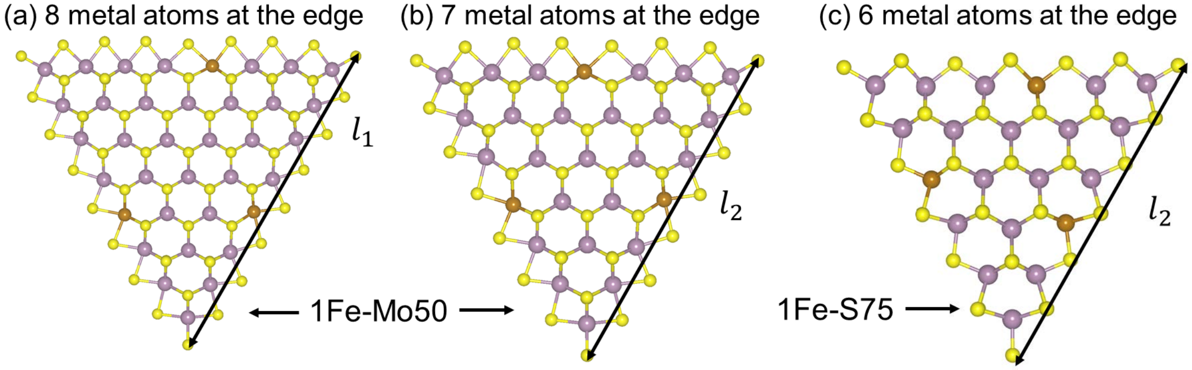

**Figure S1.** Examples of triangular flake models of $MoS_2$ ML, used for the calculation of edge formation energy, with side length $l_1$ and $l_2$ ; all three sides (edges) and vertices of the triangle are assumed to be identical. Gold, yellow, and violet-grey spheres show Fe, S, and Mo atoms, respectively. For edges with 0%, 50%, 100% S-coverages, we used two triangular flakes with (a) 8 and (b) 7 metal atoms at the edge. For edges with 75% S-coverage, we used two triangular flakes with (a) 8 and (c) 6 metal atoms at the edge.

To determine thermodynamically-favored edges of Fe-doped $MoS_2$ ML, we calculated the edge formation energy ($\gamma$), as a function of change in the chemical potential of sulfur relative to its bulk phase ($\Delta\mu_S = \mu_S - \mu_{S,bulk}$), using a triangular flake model of $MoS_2$ ML with three identical sides (or edges) of length $l$ (Figure S1).[1,2] The triangular flake has three identical edges (sides) and vertices. Therefore, the excess energy of the triangular $MoS_2$ ML flake, $\gamma_{flake}$ , is given by

$$\gamma_{flake} = 3 \times l \times \gamma + 3 \times \gamma_{vertex}, \quad \text{and} \tag{S1}$$

$$\gamma_{flake} = E_{flake} + E_{ZPE} - n_{Mo} \times \mu_{Mo} - n_{Fe} \times \mu_{Fe} - n_S \times \mu_S. \tag{S2}$$

where $\gamma$ and $\gamma_{vertex}$ are the formation energies of the edges and vertices of the $MoS_2$ ML flake, respectively; $E_{flake}$, and $E_{ZPE}$ are the 0K DFT energy and zero-point energy (ZPE) of the triangular flake, respectively; $\mu_{Mo}$, $\mu_{Fe}$, and $\mu_S$ are the chemical potentials of Mo, Fe, and S atoms, respectively; and $n_{Mo}$, $n_{Fe}$, and $n_S$ are the number of Mo, Fe, and S atoms in the triangular flake model of $MoS_2$ ML, respectively. To obtain $\gamma$ as a function of $\Delta\mu_S = \mu_S - \mu_{S,bulk}$, we apply the following thermodynamic constraints:[3,4]

$$\mu_{MoS_2} = \mu_{Mo} + 2\mu_S \,, \tag{S3}$$

$$\mu_{FeS_2} = \mu_{Fe} + 2\mu_S \text{ , and} \tag{S4}$$

$$\Delta H_{f,FeS_2}/2 < \Delta\mu_S < 0; \Delta H_{f,FeS_2} = -1.54\ eV \tag{S5}$$

where $\mu_{S,bulk}$, $\mu_{MoS_2}$ and $\mu_{FeS_2}$ are the chemical potentials of bulk sulfur, $MoS_2$ ML, and $FeS_2$, respectively, and $\Delta H_{f,FeS_2}$ is the heat of the formation of bulk $FeS_2$. To maintain the thermodynamic equilibrium of the Fe-doped $MoS_2$ ML, $\Delta\mu_S$ is subject to the constraint $\Delta H_{f,FeS_2}/2 < \Delta\mu_S < 0$; for the undoped $MoS_2$ ML, equilibrium requires that $\Delta H_{f,MoS_2}/2 < \Delta\mu_S < 0$, with $\Delta H_{f,MoS_2} = -2.66\ eV$. From Equations 1 and 2, $\gamma_{flake}$ is seen to be a linear function of the edge length $(l)$ of the model, whereas $\gamma_{vertex}$ is an additive constant. Therefore, we used two triangular $MoS_2$ ML flakes with different edge lengths $l_1$ and $l_2$ $(l_1 > l_2)$ and calculated $\gamma$ as

$$\gamma = \frac{\Delta E_{flake} + \Delta E_{ZPE} - \Delta n_{Mo}\ \mu_{MoS_2} - \Delta n_{Fe}\ \mu_{FeS_2} + (2\Delta n_{Mo} + 2\Delta n_{Fe} - \Delta n_S)\mu_S}{3\times(l_1 - l_2)}, \tag{S6}$$

where $\Delta E_{flake}$, and $\Delta E_{ZPE}$ are the differences in the 0K DFT energies and ZPE of the triangular flake model of $MoS_2$ ML with edge lengths $l_1$ and $l_2$, respectively, and may be expressed as

$$\Delta E_{flake} = E_{flake}(l_1) - E_{flake}(l_2), \tag{S7}$$

$$\Delta E_{ZPE} = E_{ZPE}(l_1) - E_{ZPE}(l_2). \tag{S8}$$

In Equation 6, $\Delta n_{Mo}$, $\Delta n_{Fe}$, and $\Delta n_S$ are the differences in the number of Mo, Fe, and S atoms in the triangular flake model of $MoS_2$ ML with edge lengths $l_1$ and $l_2$, respectively.

**(a) Undoped $MoS_2$ ML Edges** **(b) 1Fe-doped $MoS_2$ ML Edges**

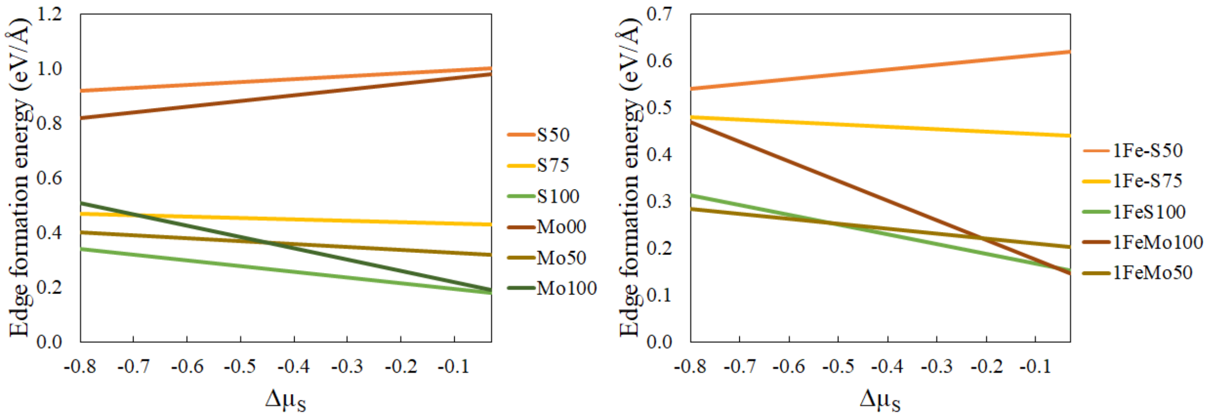

**(c) 2Fe-doped $MoS_2$ ML Edges** **(d) FullFe-doped $MoS_2$ ML Edges**

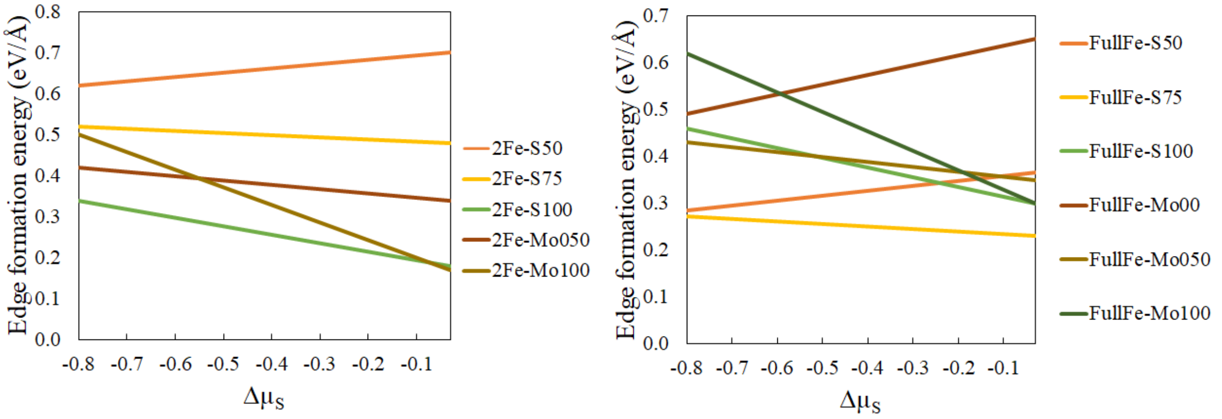

**Figure S2**. Edge formation energy of select (a) undoped $MoS_2$ ML edges, (b) 1Fe-doped $MoS_2$ ML edges, (c) 2Fe-doped $MoS_2$ ML edges, (d) FullFe-doped $MoS_2$ ML edges, as a function of change in chemical potential of sulfur, $\Delta\mu_S$, where $-0.77 \leq \Delta\mu_S \leq 0$.

## Calculation of the Free Energy of the Electrochemical Desulfurization Reaction (DSR)

The free energy of DSR on $MoS_2$ edges, $\Delta G_{DSR}$ is calculated as

$$\Delta G_{DSR} = (E_{V_s} + E_{H_2S(g)} - E_{H_2(g)} - E_{*S}) + \Delta E_{ZPE} - T\Delta S, \tag{S9}$$

$$\Delta E_{ZPE} = E_{ZPE,V_s} + E_{ZPE,H_2S(g)} - E_{ZPE,H_2(g)} - E_{ZPE,{}^*S}, \tag{S10}$$

$$\Delta S = S_{vib,V_s} + S^o_{H_2S(g)} - S^o_{H_2(g)} - S_{vib,{}^*S}, \tag{S11}$$

where $E_{*S}$, $E_{V_s}$, $E_{H_2(g)}$ and $E_{H_2S(g)}$ are the 0K DFT energies of defect-free $MoS_2$ ML, $MoS_2$ ML with a $V_S$, isolated $H_{2(g)}$ molecule, and isolated $H_2S_{(g)}$ molecule, respectively; $\Delta E_{ZPE}$ and $\Delta S$ are the differences between the zero-point energies and entropies of products ($MoS_2$ ML with a $V_S$ and $H_2S_{(g)}$) and reactants (defect-free $MoS_2$ ML and $H_{2(g)}$), respectively; T is the temperature (T=300K); $S_{vib,V_s}$, and $S_{vib,{}^*S}$ are the vibrational entropies of $MoS_2$ ML with a $V_S$ and defect-free $MoS_2$ ML, respectively; $S^o_{H_2S(g)}$ and $S^o_{H_2(g)}$ are the standard entropies of $H_2S$ and $H_2$ gas molecules, respectively.

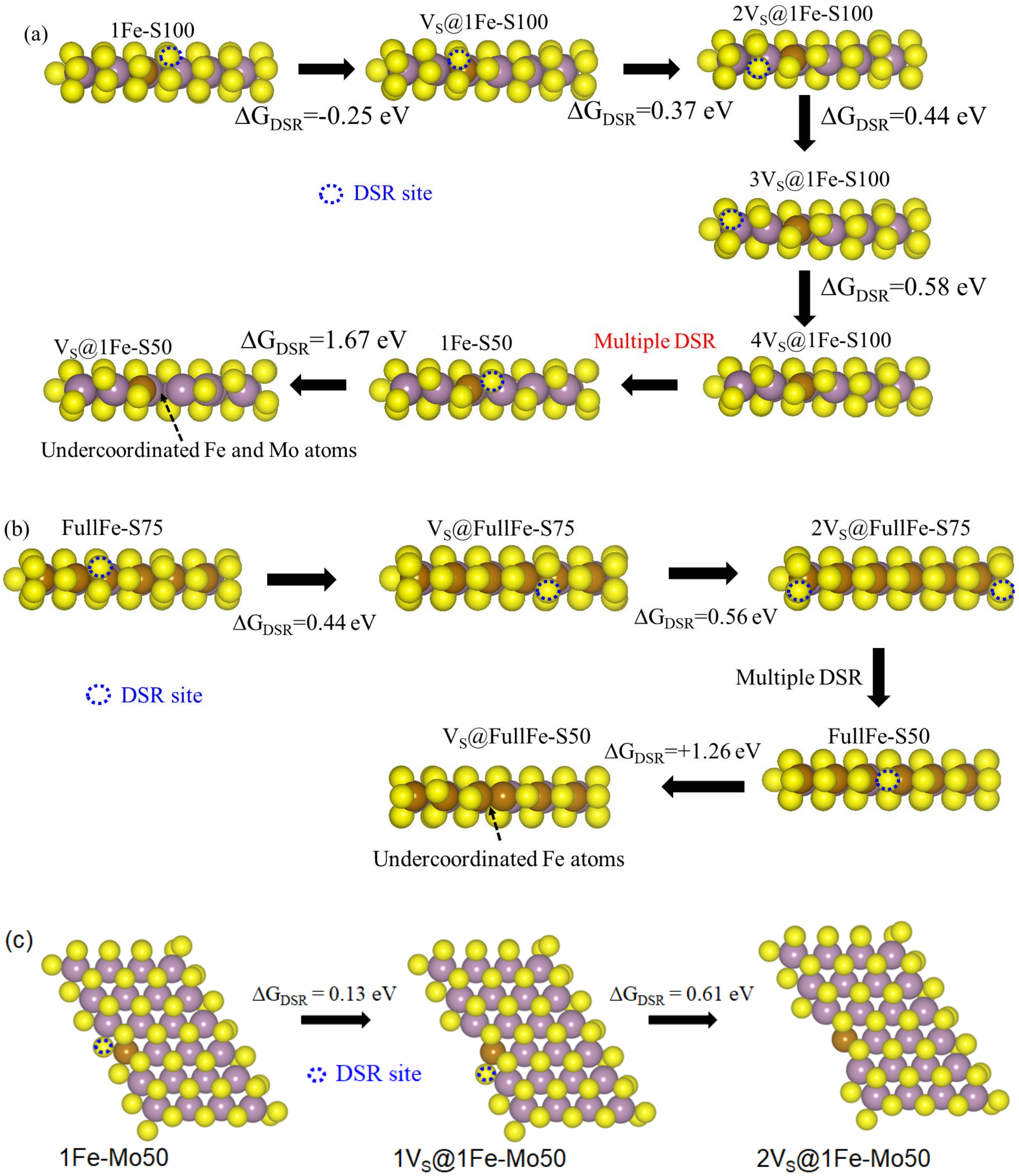

**Figure S3**. Formation of multiple sulfur vacancies via DSR to produce (a) $V_S$@1Fe-S50 from 1Fe-S100, (b) $V_S$@FullFe-S50 from FullFe-S75, and (c) $2V_S$@1Fe-Mo50 from 1Fe-Mo50 edges. Gold, violet-grey, and yellow spheres represent the Fe, Mo, and S atoms, respectively.

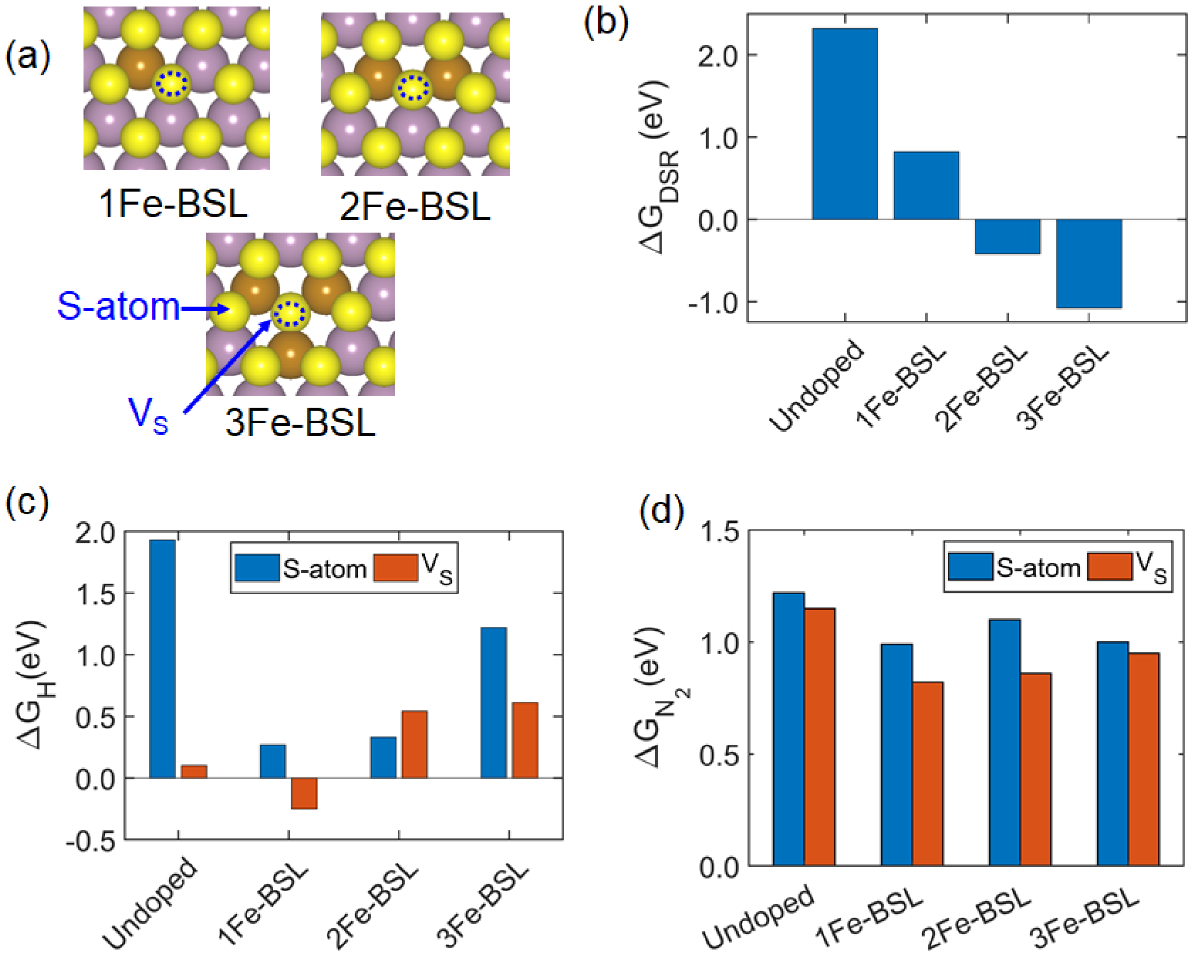

**Figure S4**. (a) S atom and $V_S$ sites on the 1Fe-doped (1Fe-BSL), 2Fe-doped (2Fe-BSL) and 3Fe-doped (3Fe-BSL) MoS2 ML basal plane. (b) $\Delta G_{DSR}$ for 1st S-vacancy formation on undoped, 1Fe-BSL, 2Fe-BSL and 3Fe-BSL $MoS_2$ ML basal plane. (c) $\Delta G_H$, and (d) $\Delta G_{N_2}$ at S atom and $V_S$ on undoped, 1Fe-BSL, 2Fe-BSL and 3Fe-BSL $MoS_2$ ML basal plane.

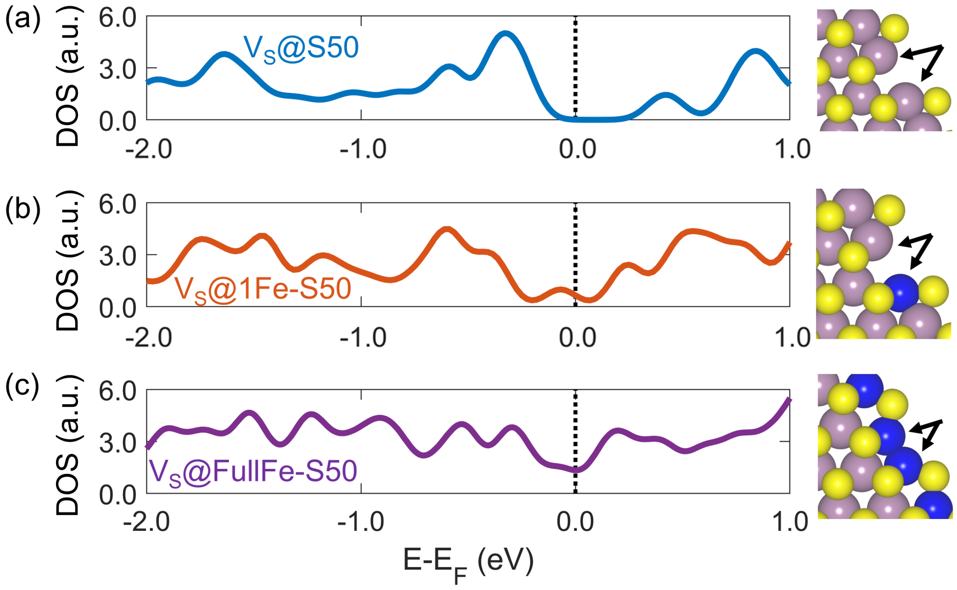

**Figure S5.** The total density of states (DOS) of the exposed two metal atoms (the $N_2$ adsorption site) at the (a) $V_S$@S50, (b) $V_S$@1Fe-S50, and (c) $V_S$@FullFe-S50 sites. Black arrows (in the right column) show the $N_2$ adsorption sites, Mo-Mo, Mo-Fe, and Fe-Fe, at the $V_S$@S50, $V_S$@1Fe-S50, and $V_S$@FullFe-S50 sites, respectively. Blue, violet-grey, and yellow spheres represent the Fe, Mo, and S atoms, respectively.

## Effect of Fe-doping on the Electronic Structure of $MoS_2$ Edges

To understand further the effect of Fe doping on the electronic structure of $MoS_2$ edges, we compared the total density of states (DOS) of $V_S$@1Fe-S50, $V_S$@FullFe-S50, and 2$V_S$@1Fe-Mo50 sites with their respective undoped counterparts, $V_S$@S50 and 2$V_S$@Mo50 (Figure S5 and S6). The undoped $V_S$@S50 site is semiconducting with a small electronic bandgap, as there are no electronic states around the Fermi level (Figure S5). The $V_S$@1Fe-S50 and $V_S$@FullFe-S50 sites, on the other hand, are metallic which shows that new electronic states emerge near the Fermi level of the $V_S$@S50 site after Fe doping. The undoped 2$V_S$@Mo50 is also metallic and after Fe doping, the 2$V_S$@1Fe-Mo50 site shows even higher DOS at the Fermi level ($E_F$) than the 2$V_S$@Mo50 site (Figure S6). Overall, we conclude that Fe doping of $MoS_2$ increases the number of electronic states at the Fermi level and improves the metallic nature of S-vacancy sites at both S50 and Mo50 edges.[5–9]

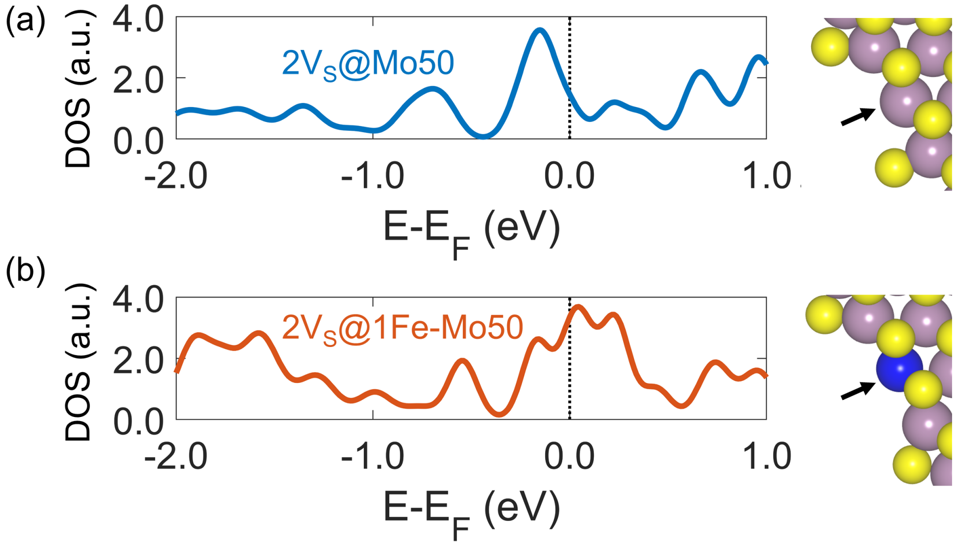

**Figure S6.** The total density of states (DOS) of the exposed metal atom (the N$_2$ adsorption site) at the (a) 2V$_S$@Mo50, and (b) 2V$_S$@1Fe-Mo50 sites. Black arrows (in the right column) show the N$_2$ adsorption sites, Mo and Fe atoms at the V$_S$@Mo50, and V$_S$@1Fe-Mo50 sites, respectively. Blue, violet-grey, and yellow spheres represent the Fe, Mo, and S atoms, respectively.

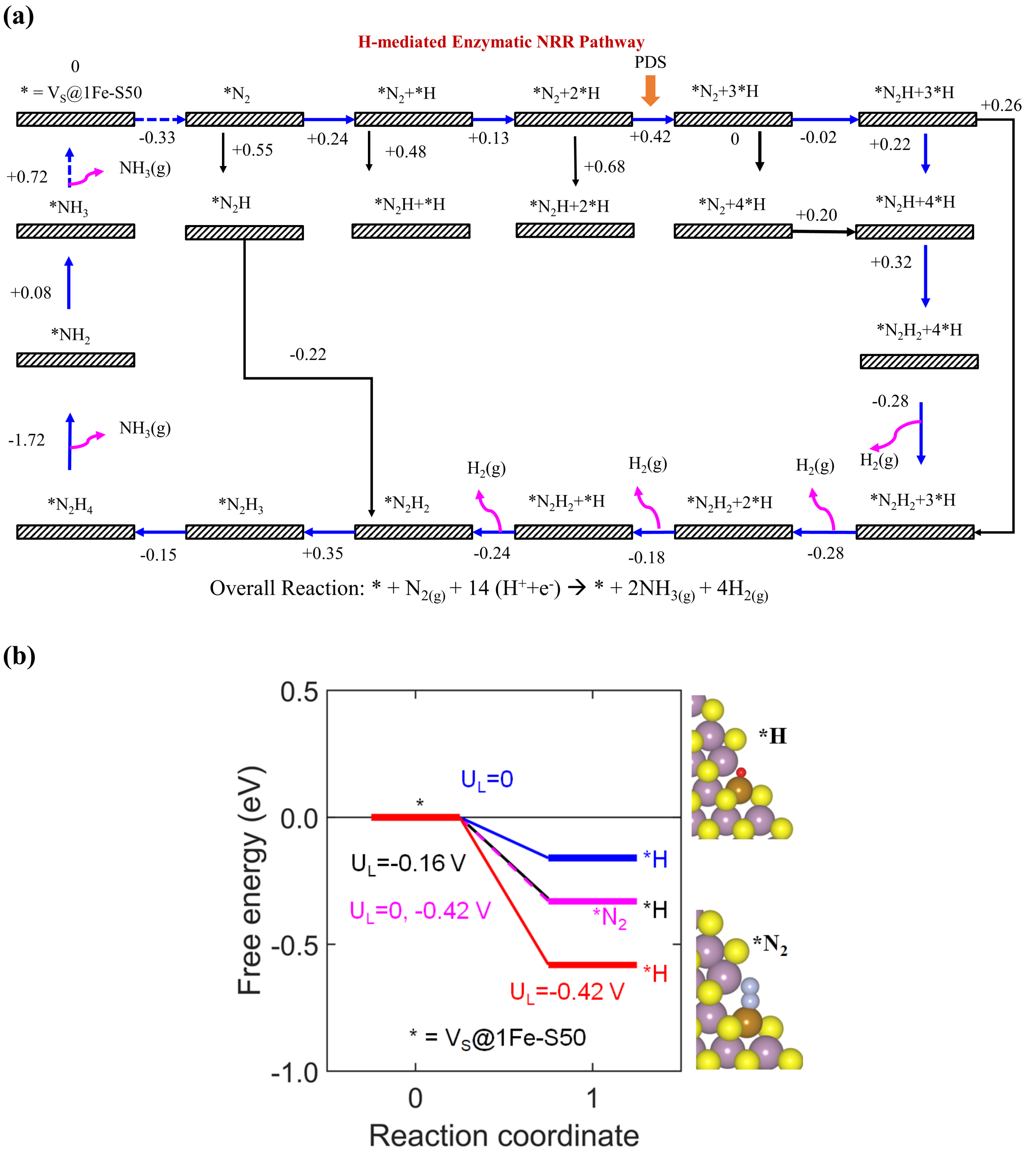

**Figure S7.** (a) Reaction network for NRR at the V$_S$@1Fe-S50 site (at U$_L$=0, low overpotential): the most favorable, H-mediated enzymatic pathway is shown by blue arrows; solid and dashed arrows show faradaic and non-faradaic steps, respectively; black arrows show steps with higher free-energy change (ΔG); values of ΔG (in eV) are indicated for each reaction step. (b) Free-energy diagram of *H, and *N$_2$ formation on the V$_S$@1Fe-S50 site at U$_L$=0, -0.16 and -0.42 V (vs RHE); non-faradic and faradic reaction steps are connected by dashed and solid lines, respectively; structural models on the right display the optimized structures of the adsorbed H atom (*H) and N$_2$ molecule (*N$_2$) on the V$_S$@1Fe-S50 site.

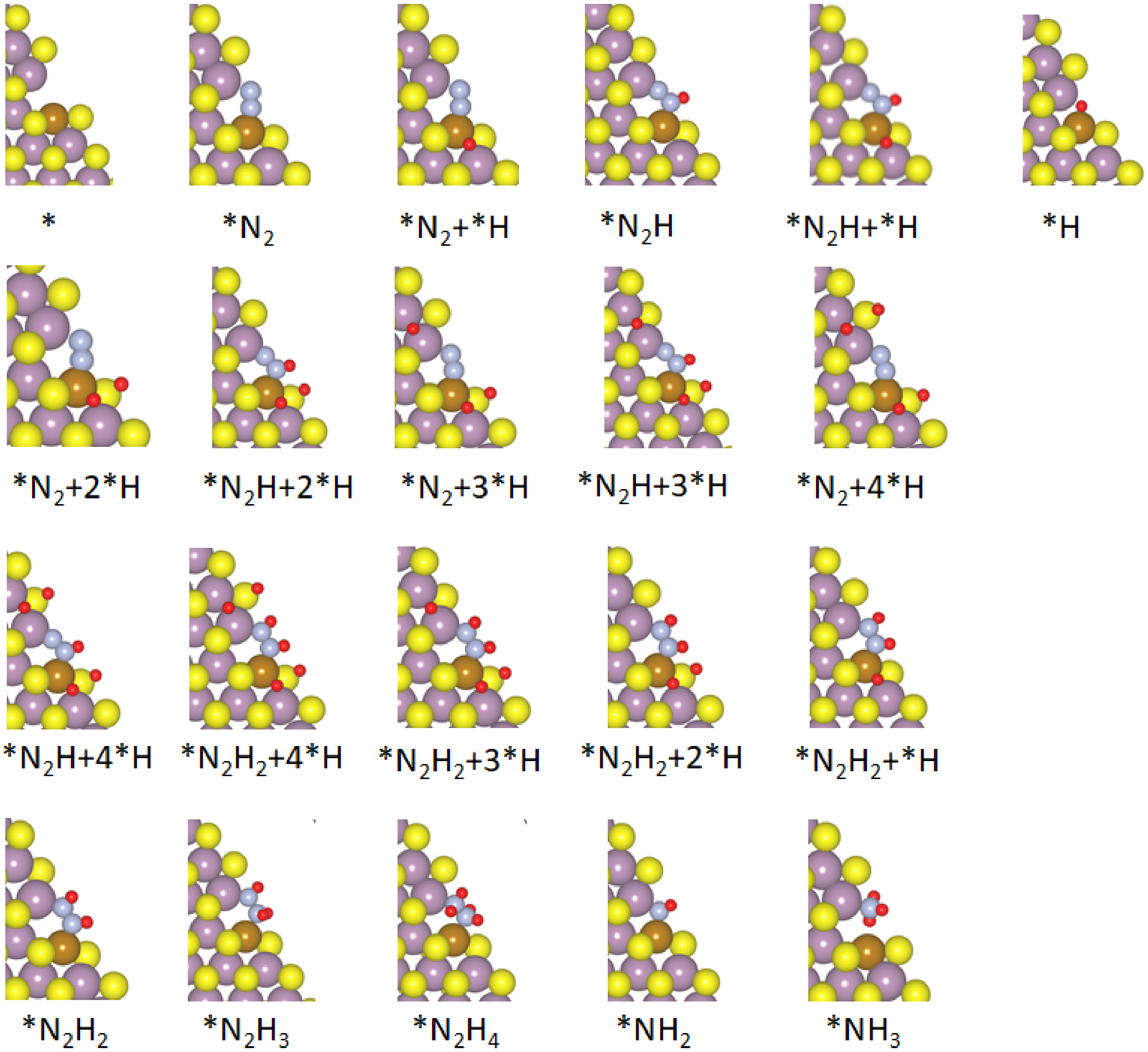

$^*$ $^*N_2$ $^*N_2+^*H$ $^*N_2H$ $^*N_2H+^*H$ $^*H$

$^*N_2+2^*H$ $^*N_2H+2^*H$ $^*N_2+3^*H$ $^*N_2H+3^*H$ $^*N_2+4^*H$

$^*N_2H+4^*H$ $^*N_2H_2+4^*H$ $^*N_2H_2+3^*H$ $^*N_2H_2+2^*H$ $^*N_2H_2+^*H$

$^*N_2H_2$ $^*N_2H_3$ $^*N_2H_4$ $^*NH_2$ $^*NH_3$

**Figure S8**. Top view of the $V_S$@1Fe-S50 site with various NRR intermediates corresponding to the reaction network in Figure S5. Gold, red, violet-grey, yellow, and silver spheres represent the Fe, H, Mo, S, and N atoms, respectively.

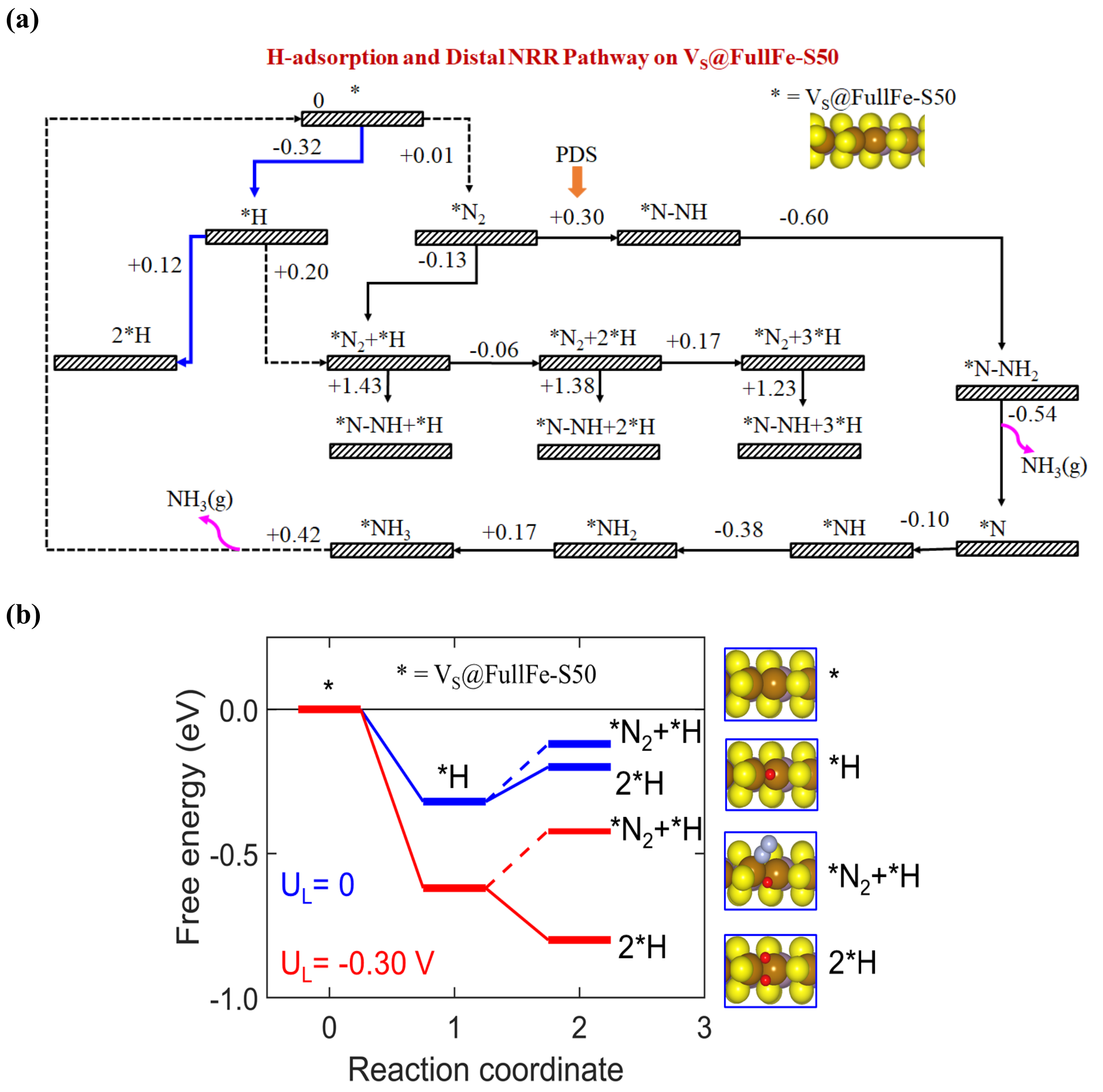

**Figure S9**. (a) Reaction network for H adsorption and NRR at the V$_S$@FullFe-S50 site (at U$_L$=0, low overpotential). Blue solid arrows indicate the most favorable steps; solid and dashed arrows show faradaic and non-faradaic steps, respectively. Values of ΔG (in eV) are indicated for each reaction step. (b) Free-energy diagram of *H, 2*H, and *N$_2$+*H formation on the V$_S$@FullFe-S50 site at U$_L$=0 V (blue) and U$_L$ = -0.30 V (red), where U$_L$ is the applied limiting potential (vs. RHE). Non-faradaic and faradaic reaction steps are connected by dashed and solid lines, respectively. Structural models on the right show the optimized structures of the clean adsorption site (*), adsorbed H atom (*H), co-adsorbed N$_2$ molecule and H atom (*N$_2$+*H), and two co-adsorbed H-atoms (2*H). Gold, red, violet-grey, yellow, and silver spheres represent the Fe, H, Mo, S, and N atoms, respectively.

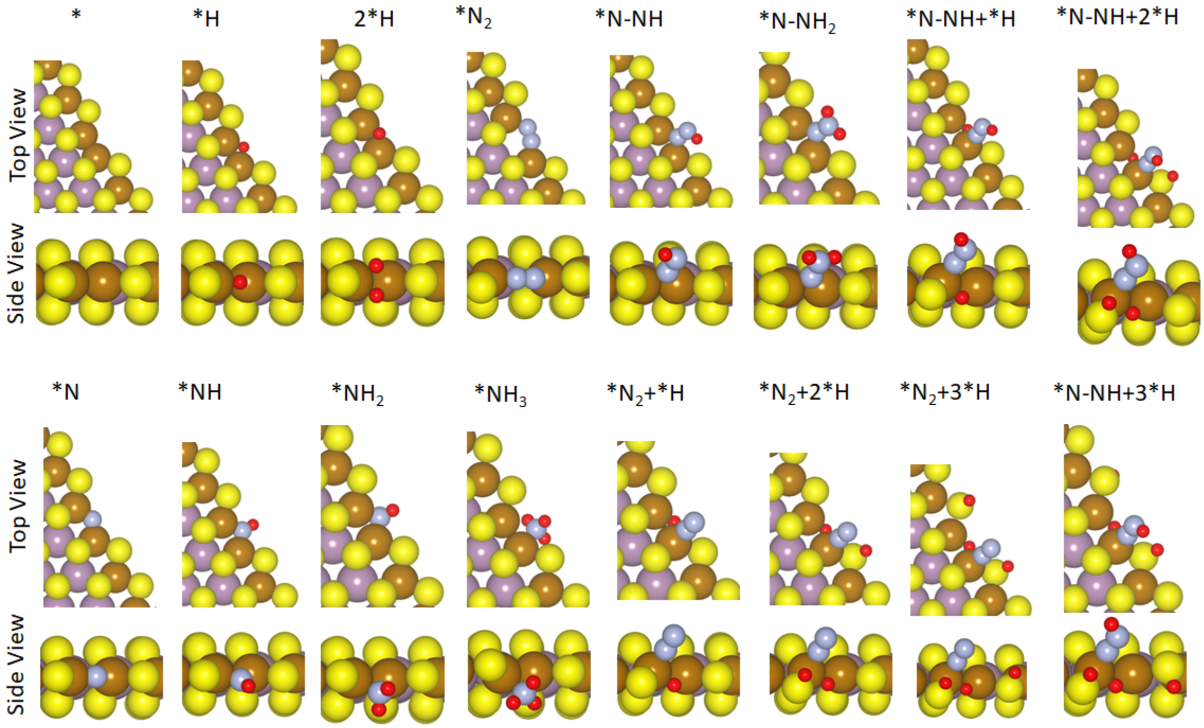

**Figure S10**. Top and side view of the $V_S$@FullFe-S50 site with various NRR intermediates corresponding to the reaction network in Figure S9. Gold, red, violet-grey, yellow, and silver spheres represent the Fe, H, Mo, S, and N atoms, respectively.

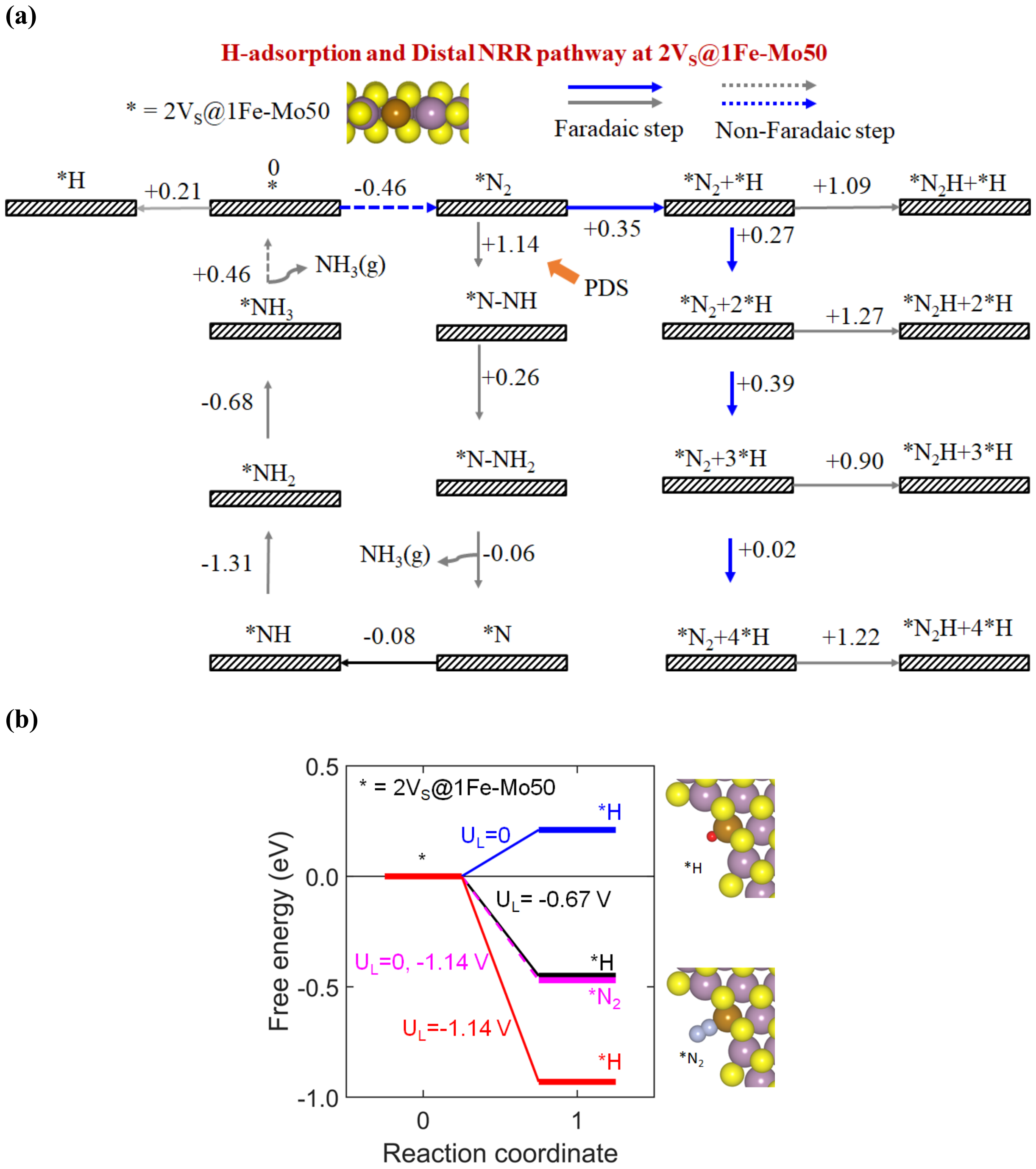

**Figure S11**. (a) Reaction network for NRR with co-adsorbed H atoms at $2V_S$@1Fe-Mo50 at $U_L$=0 (low overpotential). Blue arrows show the most favorable steps. Solid and dashed arrows show faradaic and non-faradaic steps, respectively. Grey arrows show steps with higher free-energy-change (ΔG). Values of ΔG (in eV) are indicated for each reaction step. (b) Free-energy diagram of *H and *$N_2$ formation on the $2V_S$@1Fe-Mo50 site at $U_L$=0, -0.67 and -1.14 V (vs RHE). Non-faradaic and faradaic reaction steps are connected by dashed and solid lines, respectively. The panel on the right shows the optimized structures of the adsorbed H atom (*H) and $N_2$ molecule (*$N_2$) on $2V_S$@1Fe-Mo50. Gold, red, violet-grey, yellow, and silver spheres represent the Fe, H, Mo, S and N atoms, respectively.

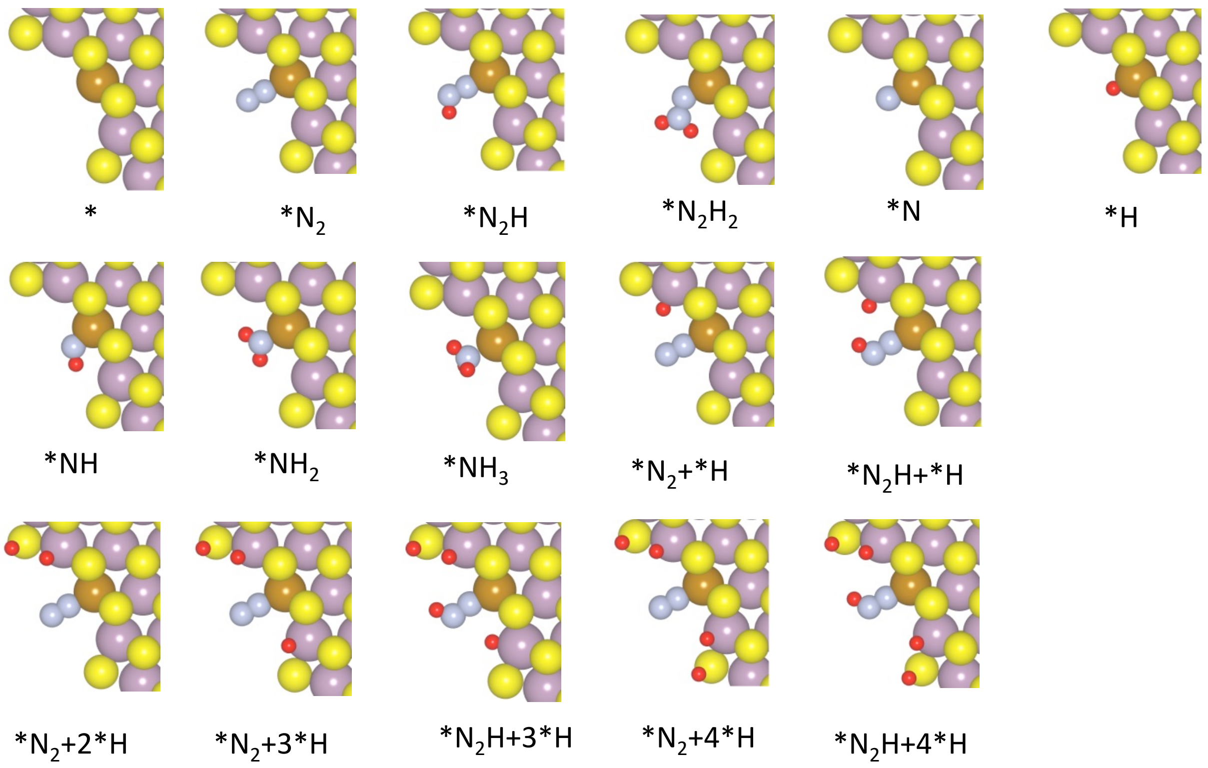
*, $*N_2$, $*N_2H$, $*N_2H_2$, $*N$, $*H$

$*NH$, $*NH_2$, $*NH_3$, $*N_2$+$*H$, $*N_2H$+$*H$

$*N_2$+2$*H$, $*N_2$+3$*H$, $*N_2H$+3$*H$, $*N_2$+4$*H$, $*N_2H$+4$*H$

**Figure S12**. Top view of the $2V_S$@1Fe-Mo50 site with various NRR intermediates from the reaction pathway in Figure S11. Gold, red, violet-grey, yellow, and silver spheres represent the Fe, H, Mo, S, and N atoms, respectively.

# References

(1) Li, T.; Galli, G. Electronic Properties of $MoS_2$ Nanoparticles. *J. Phys. Chem. C* **2007**, *111* (44), 16192–16196.

(2) Cao, D.; Shen, T.; Liang, P.; Chen, X.; Shu, H. Role of Chemical Potential in Flake Shape and Edge Properties of Monolayer $MoS_2$. *J. Phys. Chem. C* **2015**, *119* (8), 4294–4301.

(3) Northrup, J. E.; Neugebauer, J. *Theory of the Adatom-Induced Reconstruction of the SiC(0001)Root 3x Root 3 Surface*. *Physical Review B*. 1995, pp 17001–17004.

(4) Northrup, J. E.; Froyen, S. Energetics of GaAs (100)-(2× 4) and-(4× 2) Reconstructions. *Phys. Rev. Lett.* **1993**, *71* (14), 2276.

(5) Jain, A.; Bar Sadan, M.; Ramasubramaniam, A. Promoting Active Sites for Hydrogen Evolution in $MoSe_2$ via Transition-Metal Doping. *J. Phys. Chem. C 124* (23), 12324–12336.

(6) Sun, T.; Wang, J.; Chi, X.; Lin, Y.; Chen, Z.; Ling, X.; Qiu, C.; Xu, Y.; Song, L.; Chen, W. Engineering the Electronic Structure of $MoS_2$ Nanorods by N and Mn Dopants for Ultra-Efficient Hydrogen Production. *ACS Catal.* **2018**, *8* (8), 7585–7592.

(7) Liu, P.; Zhu, J.; Zhang, J.; Tao, K.; Gao, D.; Xi, P. Active Basal Plane Catalytic Activity and Conductivity in Zn Doped $MoS_2$ Nanosheets for Efficient Hydrogen Evolution. *Electrochim. Acta* **2018**, *260*, 24–30.

(8) Zhang, X.; Zhou, F.; Zhang, S.; Liang, Y.; Wang, R. Engineering $MoS_2$ Basal Planes for Hydrogen Evolution via Synergistic Ruthenium Doping and Nanocarbon Hybridization. *Adv. Sci.* **2019**, *6* (10), 1900090.

(9) Gao, G.; Sun, Q.; Du, A. Activating Catalytic Inert Basal Plane of Molybdenum Disulfide to Optimize Hydrogen Evolution Activity via Defect Doping and Strain Engineering. *J. Phys. Chem. C* **2016**, *120* (30), 16761–16766.